

A Compact Jet at the Infrared Heart of the Prototypical Low-Luminosity AGN in NGC 1052

J.A. Fernández-Ontiveros^{1,2,3,4*}, N. López-Gonzaga⁵, M.A. Prieto^{1,2}, J.A. Acosta-Pulido^{1,2}, E. Lopez-Rodriguez⁶, D. Asmus⁷, K.R.W. Tristram⁸

¹*Instituto de Astrofísica de Canarias (IAC), C/Vía Láctea s/n, E-38205 La Laguna, Tenerife, Spain*

²*Universidad de La Laguna (ULL), Dpto. Astrofísica, Avd. Astrofísico Fco. Sánchez s/n, E-38206 La Laguna, Tenerife, Spain*

³*Istituto di Astrofisica e Planetologia Spaziali (INAF-IAPS), Via Fosso del Cavaliere 100, I-00133 Roma, Italy*

⁴*National Observatory of Athens (NOA), Institute for Astronomy, Astrophysics, Space Applications and Remote Sensing (IAASARS), GR-15236, Greece*

⁵*Leiden Observatory, Leiden University, PO Box 9513, 2300 RA Leiden, The Netherlands*

⁶*SOFIA Science Center, NASA Ames Research Center, Moffett Field, CA 94035, USA.*

⁷*School of Physics & Astronomy, University of Southampton, Southampton SO17 1BJ, UK*

⁸*European Southern Observatory, Alonso de Córdova 3107, Vitacura, Santiago, Chile*

Accepted: 2019 March 08; Revised: 2019 March 25; Received 2018 December 19

ABSTRACT

The feeble radiative efficiency characteristic of Low-Luminosity Active Galactic Nuclei (LLAGN) is ascribed to a sub-Eddington accretion rate, typically at $\log(L_{\text{bol}}/L_{\text{edd}}) \lesssim -3$. At the finest angular resolutions that are attainable nowadays using mid-infrared (mid-IR) interferometry, the prototypical LLAGN in NGC 1052 remains unresolved down to < 5 mas (0.5 pc). This is in line with non-thermal emission from a compact jet, a scenario further supported by a number of evidences: the broken power-law shape of the continuum distribution in the radio-to-UV range; the $\sim 4\%$ degree of polarisation measured in the nuclear mid-IR continuum, together with the mild optical extinction ($A_V \sim 1$ mag); and the “harder when brighter” behaviour of the X-ray spectrum, indicative of self-Compton synchrotron radiation. A remarkable feature is the steepness of the IR-to-UV core continuum, characterised by a power-law index of ~ 2.6 , as compared to the canonical value of 0.7. Alternatively, to explain the interferometric data by thermal emission would require an exceptionally compact dust distribution when compared to those observed in nearby AGN, with $A_V \gtrsim 2.8$ mag to account for the IR polarisation. This is in contrast with several observational evidences against a high extinction along the line of sight, including the detection of the nucleus in the UV range and the well defined shape of the power-law continuum. The case of NGC 1052 shows that compact jets can dominate the nuclear emission in LLAGN across the whole electromagnetic spectrum, a scenario that might be common among this class of active nuclei.

Key words: galaxies: active – galaxies: jets – galaxies: individual: NGC 1052 – infrared: galaxies – techniques: interferometric – techniques: polarimetric

1 INTRODUCTION

Low-Luminosity Active Galactic Nuclei (LLAGN) are the most common population of active nuclei, including about one third of all galaxies in the local Universe (Ho et al. 1997; Ho 2008). In spite of their name, LLAGN are not simply scaled-down counterparts ($L_{\text{bol}} \lesssim 10^{42}$ erg s⁻¹) of the brighter Seyfert nuclei and quasars, but above all they are radiatively inefficient nuclei with typical $\log(L_{\text{bol}}/L_{\text{edd}}) \lesssim -3$. Their low sub-Eddington luminosities have been ascribed to a major change in the inner accretion flow, when the low accretion rate originates a Radiatively Inefficient Accretion

Flow (RIAF) below a certain truncation radius in the disc (Narayan et al. 1995; Fabian & Rees 1995; Di Matteo et al. 2003). Further structural changes are expected at low luminosities, since the wind driven by a weak nucleus would not be able to sustain either the broad-line clouds (Nicastro et al. 2003; Elitzur & Ho 2009) or the putative AGN torus (Elitzur & Shlosman 2006; Hönig & Beckert 2007). The latter is the cornerstone of the Unified Model to explain the dichotomy between type 1 and type 2 Seyfert nuclei (Antonucci 1993; Urry & Padovani 1995), but its possible disappearance at low luminosities opens one of the most compelling questions in the field: what is the nature of the continuum emission in LLAGN?

This has been a source of debate in the recent years, partly due to the heterogeneous nature of the LLAGN class. At radio and X-ray

* E-mail: j.a.fernandez.ontiveros@gmail.com, juan.fernandez@inaf.it

wavelengths, where the host galaxy contribution is negligible, the dominant nuclear emission was early associated with non-thermal processes (Condon & Dressel 1978; O’Connell & Dressel 1978; Heckman 1980; Ho et al. 2001; Terashima & Wilson 2003). However, the optical/UV continuum and the ionisation mechanisms in LLAGN stimulated an intense discussion over the last ~ 40 years (Koski & Osterbrock 1976; Keel & Miller 1983; Filippenko 1985; Terlevich & Melnick 1985; Sugai & Malkan 2000; Maoz 2007). In the mid-IR range, the detection of silicate emission within the inner few tens of parsecs (e.g. Höning et al. 2010, Mason et al. 2012, Mason et al. 2013) and the mid-IR – X-ray ratios consistent with those in Seyfert galaxies (Asmus et al. 2015) point to the presence of circumnuclear dust in these nuclei. However, the power-law continuum found in a number of LLAGN suggests that non-thermal radiation may represent a major contribution to the energy output (Rieke et al. 1982, Ho et al. 1996, Ho 1999, Mason et al. 2012, Mason et al. 2013, Fernández-Ontiveros et al. 2012), associated with a RIAF (e.g. Nemmen et al. 2014) or a compact jet (M81 in Markoff et al. 2008; M87 in Prieto et al. 2016).

Interferometry is the only technique that allows to probe the spatial distribution of the mid-IR emission at sub-parsec scales in nearby AGN (e.g. Tristram et al. 2009; Tristram & Schartmann 2011; Burtcher et al. 2013; López-Gonzaga et al. 2014), and investigate the torus endurance at low luminosities. However, only a few LLAGN are bright enough to reach the instrumental limit of the MID-Infrared Interferometric Instrument (MIDI, correlated flux $\gtrsim 90$ mJy; Burtcher et al. 2013), located at the Very Large Telescope Interferometer (VLTI) on Cerro Paranal (Chile). This is the most sensitive interferometric instrument in the mid-IR to date. One of these sources is NGC 1052, a nearby E4 galaxy ($z = 0.0045$; $D = 18$ Mpc, $1'' \sim 87$ pc, Jensen et al. 2003) that hosts a prototypical Low-Ionisation Nuclear Emission-line Region (LINER) and has been considered a reference to define the general properties of its class (Koski & Osterbrock 1976; Fosbury et al. 1978; Heckman 1980). With a bolometric luminosity of $L_{\text{bol}} \sim 7 \times 10^{42}$ erg s $^{-1}$ and $\log(L_{\text{bol}}/L_{\text{edd}}) = -3.4$ (Fernández-Ontiveros et al. 2012, Reb et al. 2018; see Section 2.4 in this work), NGC 1052 is close to the domain of Seyfert nuclei, possibly in a transition zone between the two classes.

Observational evidences point to the presence of a nuclear absorber in this source: the detection of broad H α emission lines in polarised light from the central region (Barth et al. 1999), the high hydrogen absorption column derived from X-ray observations ($N_{\text{H}} \sim 10^{23}$ cm $^{-2}$; Hernández-García et al. 2014), and the detection of HCN molecular absorption (Sawada-Satoh et al. 2016). However, the opposite is suggested by the presence of broad components in H α and H β also in the intensity (unpolarised) spectrum (Barth et al. 1999; Sugai et al. 2005), the detection of the 9.7 μm silicate band in emission (Kaneda et al. 2008), typical of type 1 AGN, the mild $A_{\text{V}} = 1.05$ mag attenuation measured within the inner $0''.8$ in an *HST*/FOS spectrum (Dopita et al. 2015), and the variability of the nuclear UV continuum between *HST* imaging and spectra at different epochs (Maoz et al. 2005), which makes unlikely the presence of a deeply obscured nucleus in this galaxy. On the other hand, one of the most remarkable features of NGC 1052 is the shape of the nuclear continuum distribution, following a broken power law in the IR-to-UV range (Rieke et al. 1982; Becklin et al. 1982; Fernández-Ontiveros et al. 2012; Koljonen et al. 2015). This is indicative of self-absorbed synchrotron emission from a compact jet (Blandford & Königl 1979), which could dominate the overall energy output in this nucleus.

The aim of this work is to probe the mid-IR brightness distri-

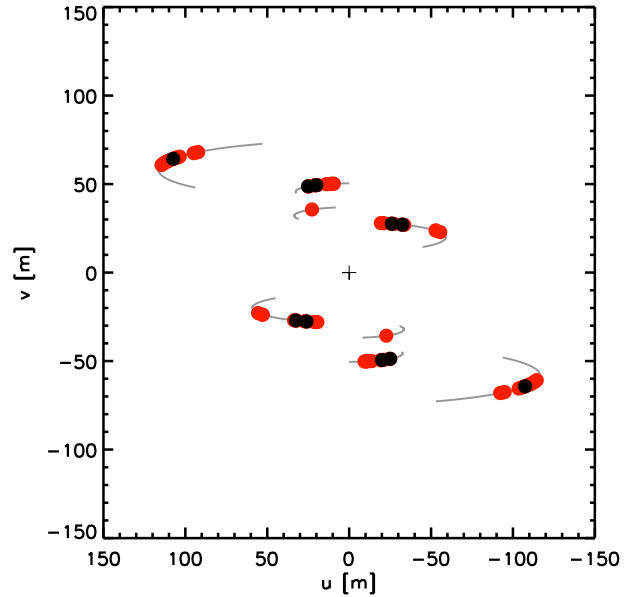


Figure 1. (u, v) coverage for NGC 1052 for the VLTI/MIDI observations. Five independent and well calibrated interferometric measurements were obtained (black dots). Data acquired at too large OPD drift values ($\gtrsim 100 \mu\text{m}$) or missing the ozone atmospheric absorption feature at $9.6 \mu\text{m}$ are flagged in red colour.

bution in the nucleus of NGC 1052 using VLTI/MIDI observations and discriminate between the proposed scenarios for the origin of this emission. That is, a nuclear IR source resolved by MIDI would imply the survival of the torus at low luminosities, while a non-thermal source is expected to be unresolved. The latter would originate in a very small region where the particles are accelerated, e.g. close to the base of the jet, the corona, or the shock location (Blandford & Königl 1979; Markoff et al. 2005; Marscher et al. 2008; Polko et al. 2014). To discern the thermal or non-thermal nature of the emission, we acquired also K_s - and N -band imaging in polarised light using the Long-slit Intermediate Resolution Infrared Spectrograph (LIRIS) at the William Herschel Telescope (WHT, 4.2 m) and CanariCam (Telesco et al. 2003) at the Gran Telescopio Canarias (GTC, 10.4 m), both facilities located at the Roque de los Muchachos Observatory (La Palma, Spain).

This work is organised as follows. In Section 2 we present the spectral flux distribution, the mid-IR interferometric observations, and the IR polarimetry for the nucleus of NGC 1052. In Section 3 we analyse the brightness distribution of the mid-IR emission in the nucleus of NGC 1052. In Section 4 we compare the case of NGC 1052 with the Circinus Galaxy – the source with the best (u, v) plane coverage using IR interferometric observations – and discuss the nature of the continuum emission on the basis of its nuclear flux distribution. The final summary and conclusions are presented in Section 5.

2 DATASET

Four different datasets are used in the present study. The first one consists of mid-IR interferometric observations acquired with VLTI/MIDI (Section 2.1), which probe the brightness distribution at the highest angular resolution available so far. The second dataset

includes *Spitzer*/IRS and VLT/VISIR¹ spectra to investigate the dust features in the mid-IR range (Section 2.2). The third dataset adds broad- and intermediate-band IR polarimetric imaging in the *K* and *N* bands. The fourth dataset is a high-angular resolution spectral flux distribution assembled using subarcsec resolution flux measurements (~ 15 – 50 pc), compared with a second flux distribution based on low-angular resolution measurements to characterise the host galaxy contamination (Section 2.4). The flux tables for both distributions are provided in Appendix A.

2.1 Mid-IR interferometry

Interferometric observations of NGC 1052 were obtained with VLTI/MIDI, a Michelson interferometer that combines the light beams from two 8.2 m Unit Telescopes (UTs) in the *N* band (8–13 μm ; Leinert et al. 2003). The instrument delivers two main interferometric observables from the interference pattern: the correlated flux spectra and the differential phases. Visibilities are derived as the ratio of the correlated flux over the total or photometric flux. However, the use of correlated fluxes is more convenient for faint sources (< 200 mJy), since measuring photometric fluxes against the fluctuations of the bright sky can be particularly challenging for these targets (Burtcher et al. 2012). Therefore in our analysis we use the measured correlated fluxes instead of the visibilities.

The MIDI interferometric campaign of NGC 1052 was carried out during the nights of August 6th and 7th, and November 2nd, 3rd, and 4th, 2014 (Programme ID: 093.B-0616, 094.B-0918). Our observing strategy, data reduction process, and analysis of the data were planned and performed using previous experience acquired during the MIDI AGN Large Programme (Burtcher et al. 2012). The low-spectral resolution NaCl prism ($R \equiv \lambda/\Delta\lambda \sim 30$) was used to disperse the light of the beams. A complete log of the observations and the instrumental setup can be found in Appendix B.

With a total flux of ~ 130 mJy at 12 μm within an aperture radius of $0''.4$ (VLT/VISIR, see Table A1), the nucleus of NGC 1052 is well below the sensitivity limit for the standard modes of MIDI. At such low fluxes, the fringe tracker can no longer follow the interferometric signal because strong noise peaks are too frequent for the group-delay tracking to stay on the MIDI fringe. Therefore we used the *no-track* mode, i.e. switching off the group-delay tracking to scan the fringes blindly. This is the only observing mode that allows the detection of faint targets below ~ 100 mJy in correlated flux. For each scan, the fringes were recorded close to the optical path delay (OPD) measured for the calibrators (HD 10380 and HD 18322), which were observed recurrently every 30–50 min. in order to correct for possible OPD drifts. The widest baselines (~ 130 m) were included in order to test the finest angular scales feasible for the UTs.

MIDI observations were processed and reduced using the *MIDI Interactive Analysis and Expert Work Station* software (MIA+EWS², Jaffe 2004), which implements the coherent integration method for MIDI data. For each measurement we derived the ratio of the target signal over the calibrator signal, which was then multiplied by the known flux of the calibrator to obtain the correlated fluxes. The spectral templates of Cohen et al. (1999) were used for the calibrators HD 10380 and HD 18322. However, further processing is needed

to correct for the correlation losses, a known bias that can be particularly severe for faint targets and cannot be corrected using the standard calibration techniques. Correlation losses are caused by the larger dispersion in the group delay estimates of weak sources when compared to the bright ones, and results in the underestimation of the correlated fluxes derived. The flux loss can be significant ($> 10\%$) for sources below 200 mJy, especially at the shortest wavelengths where the group delay error propagates into a larger phase error. To correct for correlation losses caused by the scatter in the atmospheric phase we performed *dilution* experiments as in the MIDI AGN Large Programme (Burtcher et al. 2012, Burtcher et al. 2013; see also Fernández-Ontiveros et al. 2018 for the case of IC 3639). The final (u, v) coverage is shown in Fig. 1. We obtained a total of 5 independent and well calibrated interferometric measurements (black dots). Observations obtained within 1 hour apart and sharing the same calibrator were added together using the same stacking method as that described in Burtcher et al. (2013). Data acquired at too large OPD drift values ($\gtrsim 100$ μm) are flagged in red colour in Fig. 1. Additionally, we removed those spectra where the ozone atmospheric absorption feature at 9.6 μm was not detected, following the method described in Burtcher et al. (2012). Due to the low correlated fluxes ($\gtrsim 100$ mJy) and thus the low signal-to-noise ratio (S/N), the full spectral array could not be recovered.

2.2 Mid-IR spectroscopy

Due to a refurbishment of VISIR during the interferometric campaign of NGC 1052, a simultaneous mid-IR spectrum with this instrument to double-check the single-dish total flux calibration could not be acquired. However previous VISIR spectroscopy was available in the ESO scientific archive, observed on the nights of October 21st, November 8th, and December 23rd and 24th, 2010 (PI: D. Asmus; Programme ID: 086.B-0349). These were taken in the low-resolution mode ($R \sim 350$) using the four spectral settings available prior to the VISIR refurbishment (8.5, 9.8, 11.4, and 12.4 μm). The ESO Common Pipeline Library (CPL v5.3.1, VISIR recipe v3.4.4) was used to reduce and calibrate the data (calibrators: HD 25025, HD 4128, HD 23249, and HD 8512), with further post-processing following the method described in Hönl et al. (2010). Finally, the spectrum was extracted using a $0''.75 \times 0''.52$ slit, i.e. identical to the aperture used by MIDI. The spectrum is shown in red colour in Figs 2 and 7.

Additionally, mid-IR spectra at high- and low-spectral resolution were collected from the Cornell Atlas of *Spitzer*/Infrared Spectrograph Sources (CASSIS; Lebouteiller et al. 2015). The $R \sim 600$ spectrum (PI: C. Leitherer; AOR key: 11510784) covers the 9.9–37.1 μm range with slit sizes of $4''.7 \times 11''.3$ and $11''.1 \times 22''.3$ in the SH (9.9–19.5 μm) and LH modes (18.8–37.1 μm), respectively. Fig. 2 shows the “optimal differential” spectrum extracted using the point-spread function profile (PSF; dark green). This method is optimal to recover the spectra of unresolved sources mixed with extended emission. The $R = 60$ – 130 spectrum (PI: H. Kaneda; AOR key: 18258688), shown in purple colour, corresponds to the “optimal” extraction and covers the 5.2–14.5 μm and 14.0–38.0 μm ranges with slit sizes of $3''.7 \times 57''$ and $10''.7 \times 168''$, respectively.

The infrared spectra are compared in Fig. 2 with subarcsec photometry at $\sim 0''.5$ resolution. Most of these fluxes correspond to VLT/VISIR and Gemini/T-ReCS³ observations published in the literature (see Section 2.4 for a detailed description; Table A1). Over-

¹ VLT Imager and Spectrometer for mid-InfraRed (Lagage et al. 2004).

² EWS is available for download from:

<http://home.strw.leidenuniv.nl/~jaffe/ews/index.html>

³ Thermal-Region Camera Spectrograph.

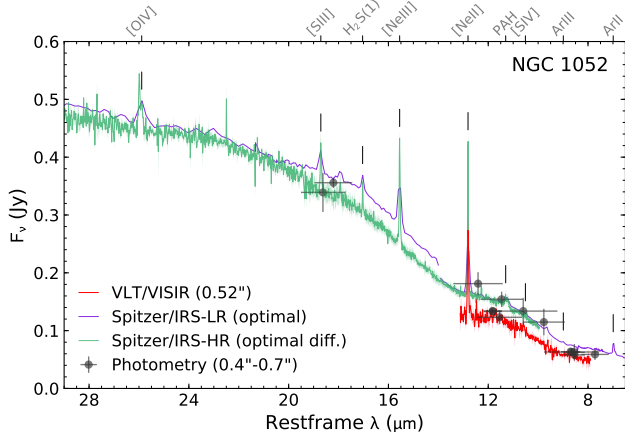


Figure 2. Nuclear IR spectra of NGC 1052 compiled from previous VISIR observations (in red) and the CASSIS database. The latter includes *Spitzer*/IRS spectra in the high-spectral resolution mode (in green; “optimal-differential” extraction) and in the low-spectral resolution mode (in purple; “optimal” extraction). The discontinuity in the low-resolution spectrum at $\sim 14 \mu\text{m}$ is possibly caused by errors in the calibration between the short-low and the long-low modules. For comparison, photometric measurements at subarcsec resolution ($0''.4\text{--}0''.7$) are also shown as black dots. The main emission lines and PAH bands are marked in the spectrum.

all, the continuum level in the three infrared spectra is in fair agreement with the photometric data, despite the large difference in the aperture sizes, up to a factor ~ 20 between *Spitzer*/IRS and VISIR at $18 \mu\text{m}$. A scatter in the mid-IR photometry of the order of $\sim 15\%$ is seen in the $10\text{--}13 \mu\text{m}$ range, possibly caused by the contribution of the polycyclic aromatic hydrocarbon (PAH) feature at $11.3 \mu\text{m}$ and the fine-structure lines of $[\text{Ne III}]_{12.8 \mu\text{m}}$ and $[\text{S IV}]_{10.5 \mu\text{m}}$ to the VISIR filters B11.7, B12.4, and B10.7, respectively. This is confirmed by the comparison of flux measurements in pure continuum emission filters –e.g. the PAH2_2 filter in VISIR for two different epochs and the Si5 filter in CanariCam, which are fully consistent within the uncertainties. The $8\text{--}13 \mu\text{m}$ continuum in the *Spitzer*/IRS spectra is $20\text{--}40 \text{ mJy}$ higher when compared to the VISIR spectrum ($\sim 15\text{--}25\%$). The silicate band at $9.7 \mu\text{m}$ is detected by both VISIR and *Spitzer* and peaks in the $10.5\text{--}11 \mu\text{m}$ range, a shift typically seen when the feature is in emission (Hatziminaoglou et al. 2015). No significant difference is detected in the strength of the silicate feature between both spectra ($S_{\text{sil}} = \ln(F_{\lambda_{\text{peak}}}/F_{\lambda_{\text{cont}}}) \sim 0.15$). The $18 \mu\text{m}$ silicate feature is detected in emission in the *Spitzer*/IRS-LR spectrum, which shows higher fluxes in this range than the IRS-HR spectrum.

2.3 IR polarimetry

To investigate further the nature of the IR emission in NGC 1052, we took advantage of the polarimetric capabilities of WHT/LIRIS and GTC/CanariCam. NGC 1052 was observed on the nights of January 14th, 2014 (Programme ID: WHT23-13B) and September 16th, 2013 (Programme ID: GTC30-13B), using the *Ks* band (cut-on at $1.99 \mu\text{m}$, cut-off at $2.31 \mu\text{m}$) and the *N* band intermediate-band filters Si2 ($\lambda_c = 8.7 \mu\text{m}$, $\Delta\lambda = 1.1 \mu\text{m}$ at 50% cut-on/off) and Si5 ($\lambda_c = 11.6 \mu\text{m}$, $\Delta\lambda = 0.9 \mu\text{m}$ at 50% cut-on/off), respectively.

Near-IR images were acquired following a dithering plus offset pattern, where the location of NGC 1052 on the detector was alternated between the centre and the sides of the detector field-of-

view. Using a Wedged Double Wollaston system (WeDoWo; Oliva 1997), LIRIS splits the light beam in four slices, delivering simultaneously four different position angles (0° , 90° , 45° , and 135°) for the polarised flux. Each acquisition had an exposure time of 25 s, and were acquired following a three-point dither pattern to improve the subtraction of the background. The total exposure time on source was 1200 s, that is 600 s for each of the two orthogonal positions of the half-wave plate, resulting in eight final images containing the information on the I, U, and Q parameters. The rotation of the retarder plate allows us to switch the positions of the ordinary and extraordinary beams on the detector, and thus cancel possible differences in the transmission along the light path. To calibrate and correct for the instrumental polarisation, two zero-polarisation standard stars (HD 14069, GD 319; Schmidt et al. (1992)) and a linearly polarised star (HD 3856C; Whittet et al. 1992) were observed during the same night. The images were reduced using the dedicated `lirisdr`⁴ package in IRAF⁵, and includes the background subtraction, alignment and combination of the individual frames. Nuclear fluxes for each frame were derived using aperture photometry ($r \sim 0''.75$), subtracting the adjacent background dominated by the underlying galaxy. The Stokes parameters (I, Q, and U) were derived from the measured fluxes following the method described in Alves et al. (2011). After correcting for the polarisation bias we measured a linear polarisation degree in the nucleus of $\sim 0.45 \pm 0.07\%$ at $\text{PA} = 169^\circ \pm 9^\circ$ in the *K* band. For the polarised standard we obtained $2.2 \pm 0.2\%$ and $75^\circ \pm 4^\circ$, in very good agreement with the $2.21 \pm 0.55\%$ and $78^\circ \pm 17^\circ$ values given by Whittet et al. (1992).

In the mid-IR, the background subtraction was performed in real time during the observations using the standard chop-nod technique, with a chop-throw of $9''$, a chop-angle oriented along the North-South axis, and a chop-frequency of 1.93 Hz. The instrumental position angle (IPA), i.e. the orientation of the detector vertical axis on the sky, was 0° East of North, and the telescope was nodded every 46 s along the chopping direction. Only one “slot” was used during the observations, i.e. one slice of the CanariCam polarimetry mask ($25''.6 \times 2''.0$). For each filter, four observing cycles were completed with a total on-source time of 1748 s and 1776 s at $8.7 \mu\text{m}$ and $11.6 \mu\text{m}$, respectively. The data were reduced following the method described in Lopez-Rodriguez et al. (2016, 2018a), which includes the correction of the I, Q, and U Stokes parameters by the instrumental polarisation, the polarisation efficiency, and the polarisation bias. Observations of the unpolarised standard star HD 16212 were used to calibrate: *i*) the instrumental linear polarisation, of about $0.6 \pm 0.1\%$ and $0.5 \pm 0.1\%$ at $8.7 \mu\text{m}$ and $11.6 \mu\text{m}$, respectively; *ii*) the shape of the PSF, characterised by a full-width at half-maximum (FWHM) of $0''.45 \times 0''.38$ with $\text{PA} = 50^\circ$ at $8.7 \mu\text{m}$ and $0''.36 \times 0''.34$ with $\text{PA} = 38^\circ$ at $11.6 \mu\text{m}$; and *iii*) the absolute flux of the mid-IR core in NGC 1052, using the catalogue fluxes given by Cohen et al. (1999). Typical flux calibration uncertainties of 15% were estimated.

Due to the limited number of mid-IR polarimetric standards for a 10 m class telescope, we used as calibrator the Herbig-Haro object HH7-11 ($\alpha = 03\text{h } 29\text{m } 3.75\text{s}$, $\delta = +31\text{d } 16\text{m } 4.0\text{s}$), which shows a *K* band linear polarisation degree of 7.24% at a position angle

⁴ <https://github.com/jacostap/lirisdr>

⁵ IRAF is distributed by the National Optical Astronomy Observatories, which are operated by the Association of Universities for Research in Astronomy, Inc., under cooperative agreement with the National Science Foundation.

PA = $56^\circ \pm 4^\circ$ (Strom et al. 1976; Tamura et al. 1988). Thus, to calibrate the PA zero-offset for the linear polarisation, HH7-11 was observed immediately before NGC 1052, with an on-source time of 146 s. To our knowledge, these are the first mid-IR polarimetric observations of HH7-11 published in the literature. Once corrected by the instrumental polarisation and the polarisation efficiency, we measure a degree of $2.8 \pm 0.4\%$ and $6.5 \pm 0.5\%$ at $8.7\ \mu\text{m}$ and $11.6\ \mu\text{m}$, respectively. The uncertainties in the degree and the PA of the polarisation were estimated following the method of Naghizadeh-Khouei & Clarke (1993), taking into account the signal-to-noise, the measured degree, and the PA values. To estimate the zero-angle, we assumed that the angle of the linear polarisation in HH7-11 is constant from $2.2\ \mu\text{m}$ to $11.6\ \mu\text{m}$, which suggests that the same mechanism dominates the polarised emission in this wavelength range. Finally, the zero-angle of the linear polarisation was obtained from the difference between the $\theta_{2.2\ \mu\text{m}} = 56^\circ$ value and our measurements of $\theta_{8.7\ \mu\text{m}} = 38^\circ \pm 6^\circ$ and $\theta_{11.6\ \mu\text{m}} = 40^\circ \pm 3^\circ$. That is, we obtain zero-offset corrections to the PA of the linear polarisation of about $\Delta\theta_{8.7\ \mu\text{m}} = 18^\circ \pm 6^\circ$ and $\Delta\theta_{11.6\ \mu\text{m}} = 16^\circ \pm 4^\circ$.

To minimise a possible contamination from extended (diffuse) warm dust emission, we measured the total and polarised fluxes for the nucleus of NGC 1052 within a $0''.5$ (42.5 pc) aperture radius. The polarisation degree and position angle measured are $4.4 \pm 0.5\%$ at $125^\circ \pm 4^\circ$ in the Si2 filter, and $3.5 \pm 0.6\%$ at $118^\circ \pm 5^\circ$ for Si5.

2.4 Spectral Flux Distribution

Flux measurements based on high-angular resolution observations are used to isolate the nuclear emission in NGC 1052 and avoid possible contamination by the host galaxy. This dataset includes $0''.2$ aperture radius photometry from near-IR adaptive optics-assisted observations with VLT/NaCo⁶ and diffraction-limited imaging with *HST* in the UV/optical range. In all cases, the local background was estimated in a surrounding annulus and subtracted from the measured fluxes. The flux distribution of NGC 1052 presented here includes a few updates with regard to previous versions introduced in Fernández-Ontiveros et al. (2012), Koljonen et al. (2015), and more recently in Reb et al. (2018). Specifically, the mid-IR range has been completed with VLT/VISIR (observations made between September 2009 and October 2010) and Gemini/T-ReCS (acquired in August 2007) flux measurements at $\sim 0''.5$ resolution from Asmus et al. (2014). In this work we also provide previously unpublished VLT/VISIR photometry with the PAH1 and PAH2_2 filters (Programme ID: 095.B-0376; PI: D. Asmus) for observations obtained with the upgraded VISIR instrument (Käufl et al. 2015; Kerber et al. 2016) using exposure times of 7 and 10 min., respectively. These include three different acquisitions between July and August 2015, and were intended to check for possible flux changes since the MIDI data were acquired. The reduction was performed with the standard ESO pipeline, and the fluxes were extracted using MIRphot (see Asmus et al. 2014). The resulting fluxes for the PAH1 (58 ± 3 mJy) and PAH2_2 filters (133 ± 3 mJy) are in agreement with previous measurements. Thus, no variability at subarcsec scales in the mid-IR range is detected between 2007 and 2015. Additionally, the unresolved nuclear source in GTC/CanariCam total intensity images ($< 0''.43 \sim 38$ pc) has a flux of 63 ± 6 mJy and 123 ± 12 mJy in the Si2 and Si5 filters, respectively, in agreement with previous VISIR and T-ReCS measurements (see Table A1).

⁶ Nasmyth Adaptive Optics System (NAOS) + Near-Infrared Imager and Spectrograph (CONICA; Lenzen et al. 2003; Rousset et al. 2003).

On the other hand, NGC 1052 is much more active in the millimetre range showing a high variability ($\sim 70\%$) at 22 and 43 GHz during a VLBI monitoring campaign (Baczko et al. 2019). The maximum and minimum fluxes measured between 2005 and 2009 have been incorporated to our high-angular resolution database. At higher frequencies we also included Atacama Large Millimeter/submillimeter Array (ALMA) measurements in the 108–353 GHz range recently published by Pasetto et al. (2019), and archival observations in the 419–478 GHz range where NGC 1052 was acquired as a calibrator (programme: 2013.1.00749.S, PI: R. Dominik). We calibrated the archival observations using CASA⁷ v4.7.2 and the scripts provided by the ALMA Observatory in the scientific archive. Four continuum bands were reconstructed using CASA v5.4.0, with briggs weighting and a robust parameter of 0.5 for the cleaning process. The synthesised beam has a size of $\sim 0''.12$ (see Table A1), thus comparable with the optical and near-IR data. The nuclear flux was measured by fitting a 2D elliptical Gaussian profile to the nuclear source, which remain unresolved in all bands.

IR-to-UV fluxes were corrected for Galactic reddening ($A_V = 0.073$ mag; Schlafly & Finkbeiner 2011), using the extinction curve from Cardelli et al. (1989) and $R_V = 3.1$. Fluxes derived from X-ray and radio interferometric observations were compiled from published values in the literature. The complete high-angular resolution flux distribution⁸ and the corresponding references are given in Table A1. Although X-ray observations do not have subarcsec resolution, a significant contamination from the underlying galaxy is not expected in this range, thus we assume that X-ray fluxes are representative of the LLAGN core. Low-angular resolution measurements ($\gtrsim 1''$; Table A2) were compiled from the NED database⁹ and the literature, and are used as a reference for the contribution of the host galaxy. A numerical integration of the high-angular resolution flux distribution plus low-angular resolution measurements in the $20\ \mu\text{m}$ – $3\ \text{mm}$ gap gives a luminosity of $5.3 \times 10^{42}\ \text{erg s}^{-1}$ for the radio-to-UV range (Reb et al. 2018), and $1.7 \times 10^{42}\ \text{erg s}^{-1}$ for the X-ray range. Thus, we adopt $L_{\text{bol}} \sim 7 \times 10^{42}\ \text{erg s}^{-1}$, which corresponds to $\log(L_{\text{bol}}/L_{\text{edd}}) = -3.4$ for a black hole mass of $1.55 \times 10^8 M_\odot$ (Woo & Urry 2002).

3 RESULTS

Despite the lack of the full spectral information (Section 2.1), a hint on the N band shape can be recovered from the average correlated fluxes at 8.5, 10.5, and $12\ \mu\text{m}$, derived for every independent (u, v) -point. Prior to the modelling in Sections 3.1 and 3.2, one can anticipate from Fig. 3 that the correlated flux does not vary significantly with the projected baseline length. A somewhat lower correlated flux at the widest baselines (130 m) might be present at $12\ \mu\text{m}$ – perhaps also at $10.5\ \mu\text{m}$ – but the difference is smaller than the error bars. This implies that the mid-IR brightness distribution in the nucleus of NGC 1052 is compact at the highest resolution provided by MIDI using the baselines available for the UTs. This compact mid-IR core dominates the total emission of the galaxy at the larger scales seen by *Spitzer* ($> 10''$) and remains unresolved even at an angular resolution about 2000 times higher.

⁷ Common Astronomy Software Applications package

⁸ Tabulated fluxes are not corrected for Galactic reddening.

⁹ The NASA/IPAC Extragalactic Database (NED) is operated by the Jet Propulsion Laboratory, California Institute of Technology, under contract with the National Aeronautics and Space Administration.

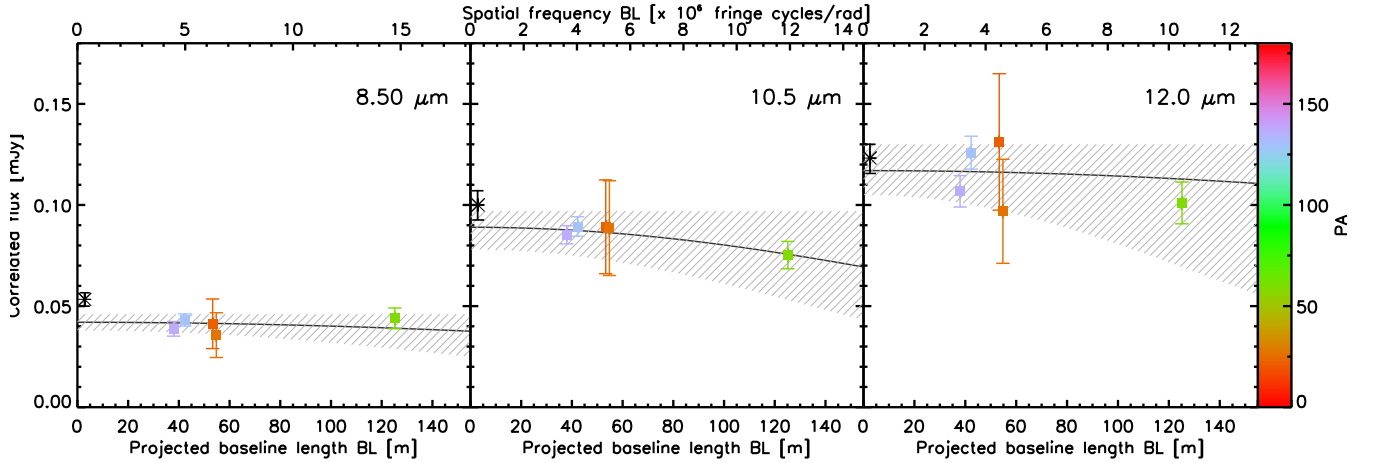


Figure 3. VLT/MIDI correlated fluxes for NGC 1052 as a function of the projected baseline length BL at $\lambda = 8.5 \mu\text{m}$ (left panel), $10.5 \mu\text{m}$ (centre), and $12.0 \mu\text{m}$ (right). Data points are colour coded based on the position angle of the corresponding projected baseline. Black asterisks at zero-metre baseline length represent the single-dish total flux measurements (see Table 1). The solid line represents the best-fit Gaussian model and the shaded region corresponds to its 1σ uncertainty area. The correlated fluxes at $8.5 \mu\text{m}$ show the presence of an unresolved source ($< 3.9 \text{ mas} \sim 0.3 \text{ pc}$) in the nucleus of NGC 1052, while at $10.5 \mu\text{m}$ and $12.0 \mu\text{m}$ the nucleus could be marginally resolved.

Table 1. Best-fit parameters obtained for a Gaussian model applied to the measured visibilities for the three wavelength bands extracted from MIDI spectra. The columns correspond to the FWHM of the Gaussian (given in mas and pc, for $D = 18 \text{ Mpc}$), the total integrated flux of the model, the best-fit reduced χ^2 , and the average continuum flux in the VISIR spectrum (the error corresponds to the standard deviation within $\pm 0.1 \mu\text{m}$ from λ). Note that uncertainties in the model fluxes do not include the calibration errors, which are expected to be of about 20–30%.

λ μm	FWHM mas	FWHM pc	Model flux mJy	Red. χ^2	VISIR spec. mJy
8.5	< 3.9	< 0.3	$42.2^{+3.3}_{-4.0}$	0.51	53 ± 3
10.5	< 5.7	< 0.5	$88.7^{+8.8}_{-13.2}$	0.12	100 ± 7
12.0	< 6.8	< 0.6	$117.2^{+12.8}_{-12.2}$	0.93	123 ± 7

3.1 Gaussian brightness distribution

Fitting the correlated fluxes with a Gaussian distribution is a common strategy to recover, at first order, the size of the mid-IR brightness distribution (Burtscher et al. 2013). Due to the limited number of interferometric measurements in NGC 1052, a simple model was used in the first analysis to avoid possible degeneracies. 2D symmetrical Gaussian distributions were fitted to each of the three wavelength bands, using two free parameters: the total flux (F_λ) and the FWHM (θ_λ). Single-dish fluxes, mainly from VISIR, were included to sample the zero-metre baseline length and constrain the total integrated flux of the nucleus (“VISIR spec.” column in Table 1 and black asterisks in Fig. 3).

The best-fit parameters obtained for the Gaussian model fit are listed in Table 1 along with their corresponding 1σ uncertainties. The radial plots of the best-fit model are shown in Fig. 3, together with the associated 1σ uncertainty region for each wavelength band. Overall, the fit suggest that the nucleus of NGC 1052 is an unresolved source even at the longest baselines. For the three bands, the total flux of the unresolved emission is well constrained, the intersection at zero-metre baseline length is found inside the 1σ error flux of the single-dish measurements at $10.5 \mu\text{m}$ and $12 \mu\text{m}$, while

at $8.5 \mu\text{m}$ the single-dish flux is slightly above the uncertainty but still compatible with the correlated flux at 130 m. On the other hand, the Gaussian FWHM is unconstrained and thus the values shown in Table 1 shall be considered as upper limits to the size of the brightness distribution. At $10.5 \mu\text{m}$ and $12.0 \mu\text{m}$ the best-fit model is somewhat compatible with a marginally resolved source. However, most of the mid-IR nuclear emission in NGC 1052 is confined within a very compact region of $< 5 \text{ mas}$ in size. At a distance of 18 Mpc, this corresponds to a size smaller than $< 0.5 \text{ pc}$.

3.2 Power-law dust distribution

A more physically motivated model was also applied to infer the dust size distribution, following the approach described in Kishimoto et al. (2007) and Kishimoto et al. (2011). The model assumes a power-law dust density distribution ($\propto r^\gamma$) down to a certain inner radius (R_{in}) where the profile is truncated due to the sublimation of the dust grains by the AGN radiation. We fixed the inner radius at $R_{\text{in}} = 9.4$ light days, which corresponds to the expected value derived from the correlation between the accretion disc luminosity (L_{UV}) and the K band reverberation measurements obtained for nearby Seyfert 1 galaxies (Suganuma et al. 2006; Kishimoto et al. 2007). Note that this radius is, at the same AGN luminosity, about 3 times lower when compared to the Barvainis (1987) sublimation radius (Kishimoto et al. 2009). The L_{UV} estimate is based on the $L_{\text{UV}}-L_X$ relation from Marchese et al. (2012), using a 2–10 keV absorption-corrected luminosity¹⁰ of $L_X \sim 4.4 \times 10^{41} \text{ erg s}^{-1}$ (Brenneman et al. 2009), which translates into $L_{\text{UV}} \sim 2.8 \times 10^{42} \text{ erg s}^{-1}$. Additionally, we assumed a dust sublimation temperature of 1500 K, a grain size of $0.05 \mu\text{m}$, and a temperature gradient index of $\beta \sim -0.36$ for the dust in the torus, assuming standard interstellar-medium dust grains ($T \propto r^\beta$; Barvainis 1987; Kishimoto et al. 2009).

For the three wavelength bands extracted from MIDI, a steep dust density profile ($\gamma \sim -0.3$ to -0.5), typical of bright AGN (Kishimoto et al. 2011), has to be assumed for the three bands in

¹⁰ Adapted to the distance used in this work.

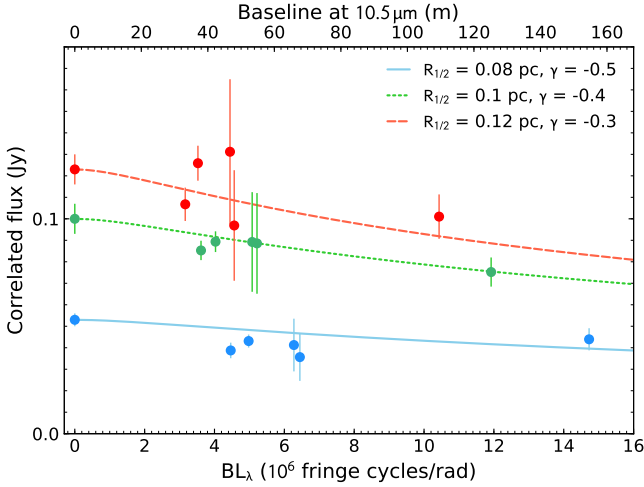


Figure 4. Best-fit power-law models to the MIDI correlated fluxes vs. baseline projected length for the nucleus of NGC 1052. The MIDI measurements have been grouped in three wavelength bands centred at 8.5 μm (blue-solid line), 10.5 μm (green-dotted line), and 12.0 μm (red-dashed line). Values obtained for the half-light radius ($R_{1/2}$) and the dust density profile index (γ) are indicated in the legend.

order to reproduce the correlated fluxes (Fig. 4). A more extended brightness distribution would have been clearly resolved with the widest baselines. Even for the longest wavelengths, the half-light radius is $R_{1/2} = 0.12$ pc, i.e. only about 15 times the size of the inner radius. If a lower X-ray luminosity is adopted, e.g. $L_X \sim 1.4 \times 10^{41}$ erg s $^{-1}$ (González-Martín et al. 2009), a smaller inner radius of $R_{\text{in}} = 4.8$ light days and a flatter dust density distribution with $\gamma \sim -0.1$ would result in a similar $R_{1/2}$ value, since the radial brightness distribution would be then dominated by the temperature profile in this case. If the limit for large grains is considered ($\beta = -0.5$), the brightness distribution at 12 μm would not be marginally resolved unless an increasing dust density profile with increasing radius ($\gamma \gtrsim 1$) is adopted. Overall, the results obtained with the power-law model are in agreement with the Gaussian analysis, i.e. *if dust emission represents a significant contribution to the mid-IR nuclear flux in NGC 1052, this must be confined within the innermost few tenths of parsec (less than 6 sublimation radii).*

3.3 IR polarisation

In Table 2 we compile the IR to UV polarisation measurements for the nucleus of NGC 1052, including our measurements and values published in the literature. The first optical polarimetric observations of NGC 1052 were presented by Heeschen (1973) in the UV range, reporting a linear polarisation degree of $3.28 \pm 0.45\%$ at PA = 42° within a $10''.2$ aperture diameter in the *U* band, and Rieke et al. (1982) in the *K* band, who measured a $0.81 \pm 0.16\%$ degree at PA = 140° within a $7''.8$ beam (i.e. an intrinsic degree of 4.5%, after the subtraction of the unpolarised stellar light contribution). Note that the angle of the linear polarisation changes about 60° – 80° from optical to IR wavelengths.

The polarisation degree measured in our two *N* band filters are in agreement within the uncertainties. In contrast, the polarisation degree measured in the *K* band is a factor of ~ 8 – 10 lower, while its PA differs by $\sim 45^\circ$ – 50° when compared to that in the *N* band (Table 2). Since the *K* band polarisation degree may be seriously

Table 2. Linear polarisation measurements for the nucleus of NGC 1052 in the IR to UV range. Note that Rieke et al. (1982) derive an intrinsic polarisation degree of 4.5% in the *K* band from the measured 0.81% after the subtraction of the unpolarised stellar light.

Band	λ_c μm	Aper. radius	P_{lin} %	PA deg	Ref.
<i>U</i>	0.38	$5''.1$	3.28 ± 0.45	42	Heeschen 1973
<i>Ks</i>	2.15	$0''.75$	0.45 ± 0.07	169 ± 9	This work
<i>K</i>	2.2	$3''.9$	0.81 ± 0.16	140	Rieke et al. 1982
Si2	8.7	$0''.5$	4.4 ± 0.5	125 ± 4	This work
Si5	11.6	$0''.5$	3.5 ± 0.6	118 ± 5	This work

affected by the contribution of unpolarised stellar light, one can estimate the intrinsic degree of polarisation by comparing the nuclear fluxes using a $0''.75$ aperture radius and those obtained at the highest angular resolution ($0''.15$), both measured in the NaCo image (see Tables A2 and A1, respectively). The former includes a factor of ~ 10.6 higher flux, thus considering this dilution factor and assuming that all the polarised radiation is originated in the unresolved core, an intrinsic linear polarisation degree of $4.8 \pm 0.7\%$ in the *K* band is estimated. This would be in agreement with the intrinsic 4.5% derived by Rieke et al. (1982), albeit the difference in the PA is still large (29°). These authors obtain the intrinsic value from the observed degree of 0.81% within a $7''.8$ beam, after subtracting the underlying galaxy. Note that our LIRIS measurement of 0.45% within a diameter of $1''.5$ has been corrected for the polarisation bias, while Rieke et al. (1982) do not mention such correction in their reported value. This could explain the difference in the observed polarisation degree and PA, and the agreement in the intrinsic degree derived in both cases.

Figure 5 shows the total intensity maps in the 8.7 and 11.6 μm filters with the corresponding nuclear polarisation vector overplotted (black line). In both filters NGC 1052 appears as a point-like source with a very faint extended tail to the NW. The latter however is not detected in the images by VISIR or T-ReCS. The angular separation between the radio jet axis at PA = 70° (white-dashed line; Kadler et al. 2004) and the IR polarisation angle is of about 35° in the *K* band and $\sim 50^\circ$ in the *N* band, and could be caused by Faraday rotation of the polarised radiation at radio wavelengths (Kadler et al. 2004), similar to the case of M87 (Avachat et al. 2016). A polarisation angle perpendicular to the direction of the magnetic field is expected for optically-thin synchrotron radiation, while optically-thick emission shows instead a parallel alignment (Pacholczyk 1970; Marscher 2014). When compared with previous mid-IR polarimetric measurements of AGN, NGC 1052 shows a relatively high polarisation degree (see review by Lopez-Rodriguez et al. 2018a), only exceeded by Cygnus A (Lopez-Rodriguez et al. 2018b), where the polarisation is ascribed to dichroic absorption and emission by aligned dust grains.

4 DISCUSSION

In this Section we will investigate the two main scenarios introduced in Section 1 to interpret the observations of NGC 1052. For each scenario we will address three essential aspects to understand the properties of this nucleus: the size of the mid-IR brightness distribution in the context of previous results for Seyfert nuclei, the origin of the polarised radiation, and the evidences in favour and

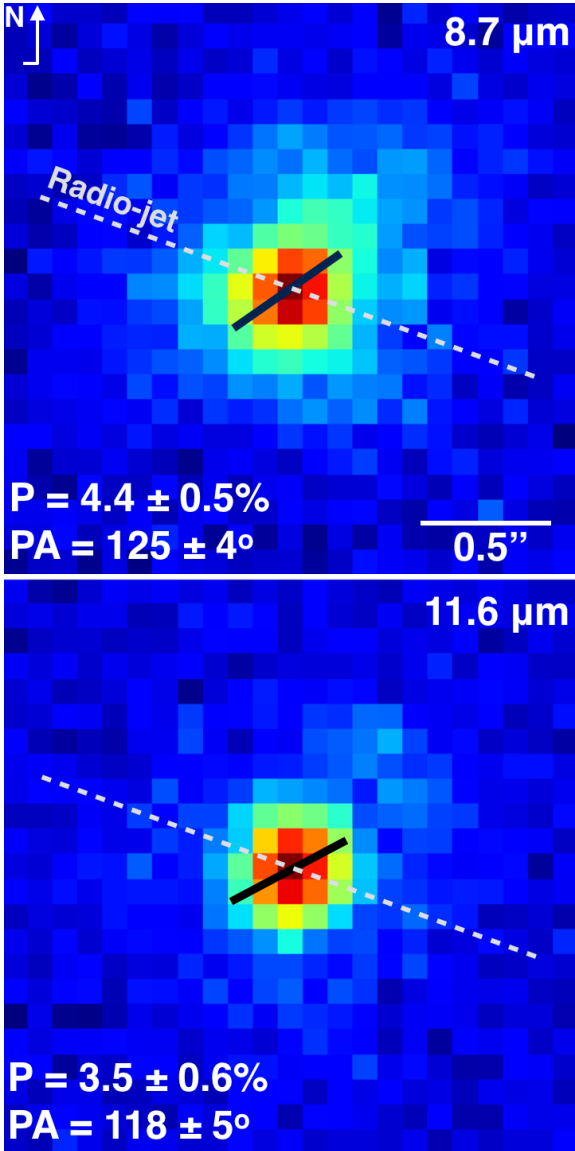


Figure 5. 8.7 μm (top) and 11.6 μm (bottom) continuum images of NGC 1052 taken with CanariCam on the 10.4-m GTC. The nuclear polarisation vector (black line) with their values (bottom left of each plot) in a $0''.5$ (42.5 pc) aperture are shown. The radio-jet (grey dashed line) with a PA = 70° (Kadler et al. 2004) is shown. North is up and East is to the left.

against the presence of a nuclear absorber. Finally, in Section 4.2 we will analyse the shape of the nuclear flux distribution, the measured optical – soft X-ray index, and the location of NGC 1052 in the mid-IR – X-ray correlation.

4.1 A very compact dust distribution

Since the mid-IR brightness distribution in NGC 1052 is confined within the innermost $\lesssim 0.5$ pc, the nuclear dust distribution cannot be resolved using the longest baselines available for the UTs (~ 130 m). This is in contrast with other nearby AGN studied by MIDI, which show extended dust distributions (e.g. López-Gonzaga et al. 2014). For a proper comparison, we estimated the sizes predicted by different calibrations based on the 12 μm nuclear luminosity. Assuming the calibration provided by Tristram & Schart-

mann (2011), for a $L_{12\mu\text{m}} = 120$ mJy (Table 1) a FWHM size of 0.5 ± 0.1 pc is expected, in marginal agreement with our upper limit of < 0.5 pc. The differences are however larger when NGC 1052 is compared with the results obtained by Kishimoto et al. (2011) in their AGN sample, where lower luminosity nuclei tend to show comparatively more extended dust distributions. Specifically, they find 12 μm half-light radii to be nearly constant around $R_{1/2} \sim 1$ pc, almost independently of the nuclear luminosity ($\propto L^{0.01}$). Following the approach in Kishimoto et al. (2011) we derive $R_{1/2} \sim 0.12$ pc for NGC 1052, i.e. nearly one order of magnitude smaller than expected.

These significant differences among the existing calibrations might be indicative of the lack of a common size–luminosity relation, as suggested by Burtscher et al. (2013). Nevertheless, a short experiment can still be performed to understand how NGC 1052 compares to the Circinus galaxy, which has been extensively studied using MIDI and is currently the object with the best (u, v) plane coverage in the mid-IR (Tristram et al. 2014). NGC 1068 has also a well sampled (u, v) plane, however the contribution of multiple shock regions located along the jet dominates the nuclear morphology in the IR, which is not shaped only by the torus emission (López-Gonzaga et al. 2014). Moreover, the system axis of the central AGN has a high inclination angle in both NGC 1052 ($\sim 72^\circ$; Kadler et al. 2004; Baczkó et al. 2016) and Circinus ($\gtrsim 65^\circ$; Greenhill et al. 2003, Zschaechner et al. 2016), i.e. the tori in these galaxies are supposed to show a nearly edge-on orientation with respect to our line of sight. Furthermore, this experiment allows us to compare the brightness distributions at shorter wavelengths, since the estimates mentioned above refer to the expected size at 12 μm .

Thus, the mid-IR brightness distribution of the Circinus Galaxy has been re-scaled to match the distance and luminosity. Fig. 6 shows the radial visibility distribution at 8.5 μm and 12 μm of the best-fit Gaussian models obtained for NGC 1052 (solid line) and Circinus at different baseline orientations (dashed lines; see fig. 5 in Tristram et al. 2014), where 17° (black-dashed line) and 137° (orange-dashed line) correspond to the most compact and the most extended axes in this nucleus, respectively. The size values for the Circinus models at different orientations have all been re-scaled by a factor of 0.5, i.e. following the size–luminosity trend at 12 μm by Tristram & Schartmann (2011) ($r \propto \sqrt{L}$; assuming a 12 μm flux of ~ 15 –20 Jy at 4 Mpc and 0.18 Jy at 18 Mpc for Circinus and NGC 1052, respectively). If instead the wavelength-dependent scaling relation found by Kishimoto et al. (2011) is adopted, the size correction factors for the case of Circinus would be of about 0.7 at 8.5 μm and ~ 1 at 12 μm . In this work we adopted the trend obtained by Tristram & Schartmann (2011) since this scenario predicts a more compact dust distribution, and thus closer to the case of NGC 1052. The left panel in Fig. 6 shows that NGC 1052 is significantly smaller than the scaled brightness distribution of Circinus at 8.5 μm , even along its more compact dimension. At 12 μm the two distributions would be marginally in agreement only along the most compact axis in Circinus (right panel), in line with the size estimated above using the correlation in Tristram & Schartmann (2011). If the two distributions were comparable, a large drop in the correlated fluxes would have been expected for any baseline orientation at 8.5 μm and for most of them at 12 μm . That is, a scaled version of the dust distribution in Circinus would have been clearly resolved by MIDI in the nucleus of NGC 1052. Therefore, from the comparison with the different torus radial structures described in Tristram & Schartmann (2011) and Kishimoto et al. (2011), and the scaling of the dust distribution in Circinus, we conclude that assuming a nucleus dominated by thermal emission in the mid-IR for NGC 1052

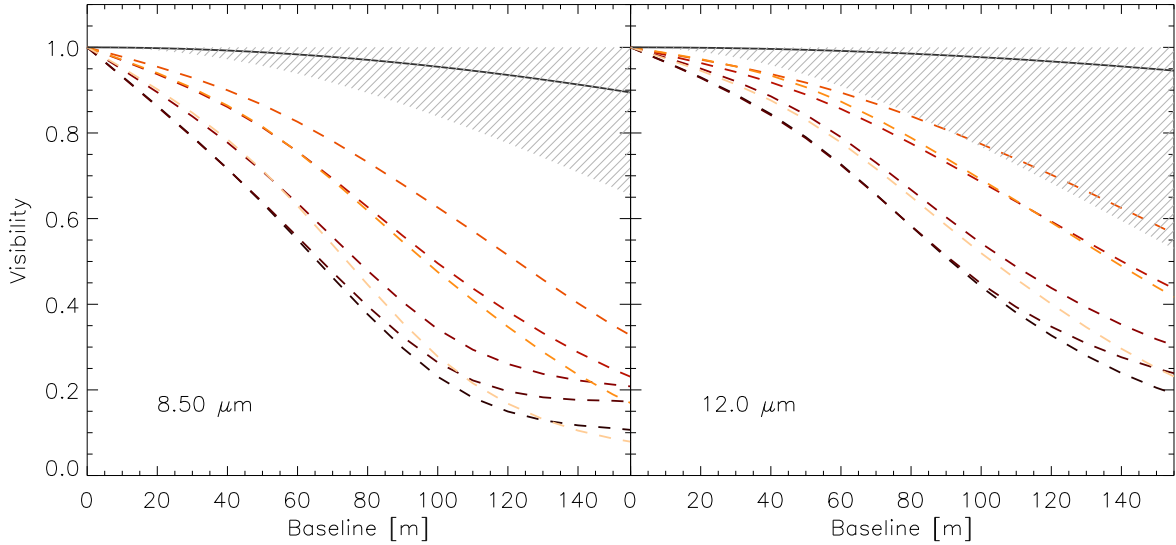


Figure 6. Visibility distribution of the Gaussian model used to fit the mid-IR correlated fluxes in NGC 1052 (black line) and the Circinus Galaxy (dashed lines; [Tristram et al. 2014](#)). The latter has been re-scaled to the distance and $12\ \mu\text{m}$ luminosity of NGC 1052 following the $r \propto \sqrt{L}$ trend derived by [Tristram & Schartmann \(2011\)](#) for a sample of Seyfert nuclei. The different colours of the dashed lines represent visibilities measured along different position angles, from the most extended axis along $\text{PA} = 137^\circ$ (black-dashed line) to the most compact one along 17° (orange-dashed line). The scaled brightness distribution in Circinus is only marginally compatible with NGC 1052 at $12\ \mu\text{m}$ along the most compact direction.

would imply an extremely compact radial dust distribution not seen in other AGN.

An important aspect that a compact dust distribution should explain is the degree of polarisation measured in the IR, which would be associated with scattering and/or dichroic absorption and emission by dust. Following the Serkowski’s law, a 4.8% degree of linear polarisation in the K band would imply an intrinsic degree of $\sim 24\%$ in the U band ([Serkowski et al. 1975](#); [Whittet 1996](#)). However, the nuclear flux is about $\gtrsim 1.5$ orders of magnitude fainter when compared to the integrated continuum in the U band within the inner $\sim 10''$ (see Fig. 7), suggesting that the 3.3% measured by ([Heeschen 1973](#)) are not caused by the nuclear polarisation. On the other hand, dust scattering would have a minor contribution in the mid-IR, where the dominant polarisation mechanisms are dichroic absorption and emission (e.g. [Lopez-Rodriguez et al. 2018b](#)). Following the relation between the degree of linear polarisation produced by the dichroic mechanism and the optical depth given by [Jones \(1989\)](#), a 4.8% degree in the K band would correspond to an opacity of $\tau_K \sim 2.8$, that is $A_V \sim 26$ mag assuming the extinction curve from [Cardelli et al. \(1989\)](#). Even under the maximum dichroic efficiency assumption (e.g. [Ramírez et al. 2014](#)), at least $A_V \gtrsim 2.8$ mag would be required to reproduce the K band polarisation.

An extinction of $A_V \sim 26$ mag would be in agreement with the presence of a dusty torus. This is also in line with the high column density of $N_{\text{H}} \sim 10^{23}\ \text{cm}^{-2}$, associated with an X-ray absorbent medium, i.e. ionised and/or neutral gas. However, three important facts point against serious absorption affecting the optical/UV range in NGC 1052: *i*) the nucleus is detected up to $2000\ \text{\AA}$ tightly following a power-law continuum with no trace of heavy absorption (Fig. 7), which would determine the shape of the spectrum in this range; *ii*) the $A_V = 1.05$ mag measured in the HST/FOS spectrum by [Dopita et al. \(2015\)](#); and *iii*) the detection of the silicate band in emission (Fig. 2), which is hard to accommodate for a nearly edge-on system. Additionally, although the presence of a broad $\text{H}\alpha$

lines in polarised light ([Barth et al. 1999](#)) proves the existence of a scattering medium, the detection of broad $\text{H}\alpha$ and $\text{H}\beta$ in the unpolarised spectrum by [Sugai et al. \(2005\)](#) also suggest a direct line of sight to the innermost nuclear region. On the other hand, NGC 1052 shows a variable N_{H} ([Hernández-García et al. 2014](#)) together with a “harder when brighter” behaviour in X-rays ([Connolly et al. 2016](#)). This means that the X-ray spectrum becomes steeper with increasing luminosity, while the opposite is expected, e.g. if one associates a larger N_{H} with an increase in the optical depth of the absorber along the line of sight.

In this context, the silicate emission feature could originate close to the active nucleus in an optically-thin dusty wind (e.g. [Keating et al. 2012](#)), or be associated with the compression of the ISM by jet-driven shocks as revealed by the detection of water masers along the radio-jet axis ([Claussen et al. 1998](#)). Alternatively, the tentative decrease in the correlated fluxes at 10.5 and $12\ \mu\text{m}$ could be indicative of extended emission on scales larger than the mid-IR core ($\gtrsim 0.5$ pc), while the nucleus remains compact at $8.5\ \mu\text{m}$. For instance, extended $9.7\ \mu\text{m}$ silicate emission in elliptical galaxies with similar strengths as in NGC 1052 has been previously reported by [Bressan et al. \(2006\)](#), and is associated with the warm dust produced by mass-losing evolved stars.

4.2 A compact jet

An alternative explanation to the compactness of the mid-IR emission is the presence of a strong non-thermal component, possibly associated with an unresolved jet. To investigate this scenario we consider the high-angular resolution spectral energy distribution (black dots in Fig. 7), along with the low-angular resolution fluxes that include the host galaxy contribution (grey spikes in Fig. 7). Nuclear fluxes swing up and down in the $0.3\text{--}3$ Jy range from $\sim 3 \times 10^8$ Hz to 100 GHz. Then they reach a turnover at $\sim 20\ \mu\text{m}$ (1.5×10^{13} Hz), followed by a well defined power-law continuum with an index of

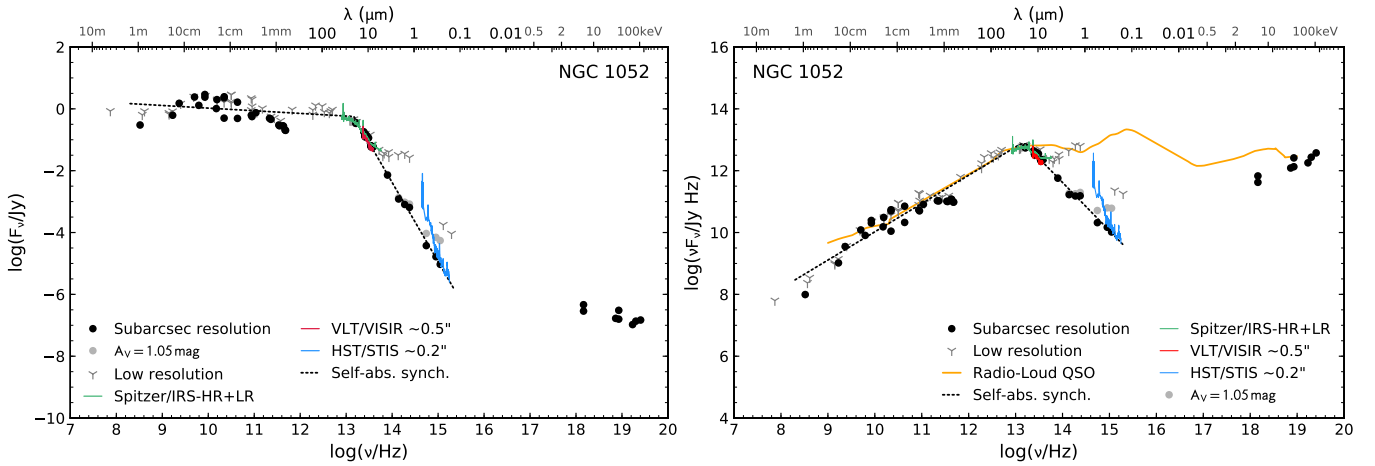


Figure 7. Rest-frame spectral flux (left panel) and spectral energy (right) distributions for the nucleus of NGC 1052 compiled for this work from high-angular resolution data ($\lesssim 0''.4$; black dots; see Table A1), and low-angular resolution measurements ($> 1''$; grey spikes; see Table A2). The $0''.2$ slit width spectrum from *HST/STIS* indicates possible variability in the optical range or galaxy starlight contamination (in blue). Nuclear fluxes corrected by an extinction of $A_V = 1.05$ mag (Dopita et al. 2015) are shown as grey circles. Flux errors are smaller than the plotted symbols and thus are not shown. The agreement among the mid-IR spectra from *Spitzer/IRS-HR+LR* ($3''.7 \times 5''.7$ aperture in the $5.2\text{--}14.5\ \mu\text{m}$ range, $4''.7 \times 11''.3$ aperture in the $10\text{--}19\ \mu\text{m}$ range, $11''.1 \times 22''.3$ aperture in the $19\text{--}37\ \mu\text{m}$ range; in green), *VLT/VISIR* ($0''.52$ slit width extraction; in red), and the subarcsec resolution photometry suggests that the nuclear emission dominates the energy output of the galaxy longwards of $\gtrsim 8\ \mu\text{m}$. The dotted line shows a broken power-law fit to the high-angular resolution data. This model should be considered only as a first order approximation of the flux distribution, since the radio-to-millimetre continuum is associated with optically-thick self-absorption synchrotron emission. In this scenario, the ripples observed below 10^{12} Hz are ascribed to optical depth effects and variability (see Baczkó et al. 2019). For comparison, the average radio-loud quasar template from Elvis et al. (1994) is also shown on the right panel (yellow-solid line).

$\alpha = 2.58 \pm 0.02$ ($S_\nu \propto \nu^{-\alpha}$; Koljonen et al. 2015; dotted line in Fig. 7). The presence of such a steep continuum was predicted in the pioneering work of Rieke et al. (1982). This shape departs largely from the big blue bump that dominates the optical/UV range in quasars (yellow-solid line in Fig. 7, right panel; Elvis et al. 1994), associated with the accretion disc emission. X-ray fluxes depart clearly for the extrapolation of the IR-to-UV power law, and are likely associated with inverse Compton radiation (Reb et al. 2018).

Longwards of $\sim 8\ \mu\text{m}$, the total flux is completely dominated by the nuclear emission, as suggested by the agreement between low- and high-angular resolution measurements. In the optical and near-IR ranges the galaxy starlight has a major contribution and only the subarcsec resolution data allow us to recover the nuclear fluxes. Note that the datasets used were acquired over several decades, in particular subarcsec IR-to-UV fluxes span a period of 18 yr. However they show a remarkably consistent shape over two orders of magnitude in frequency. Only the *HST/STIS* spectrum, extracted from a $0''.2$ slit width, shows a continuum level about 8 times higher than the flux measured in the F555W band. This could be ascribed to possible contamination by the underlying starlight, which has not been subtracted from the nuclear STIS spectrum. We also note that F555W was acquired with the Wide-Field Planetary Camera (WFPC1), thus it is affected by the spherical aberration. If we correct the F555W flux to a similar encircled energy fraction as that expected for the other *HST* bands (60–80%), the flux would increase by a factor of 3–4. Thus, the host galaxy contribution in the STIS spectrum and the light spread due to the aberration in the F555W image might explain the difference in the continuum flux between both observations.

The nuclear continuum distribution in Fig. 7 reminds closely to the characteristic pattern of self-absorbed synchrotron emission, i.e. the signature of non-thermal radiation produced by a compact jet (Blandford & Königl 1979). The radio emission shows a somewhat

flat distribution associated with optically-thick radiation, followed by a turnover and a decreasing power-law continuum with increasing frequency in the optically-thin range. Note that the power-law fit in the optically-thick domain shown in Fig. 7 should be considered only as a first order approximation, since the ripples observed in the flux distribution at frequencies < 100 GHz are likely caused by the superposition of different jet components and also by flux variability (Heeschen & Puschell 1983, Tornaiainen et al. 2007). A four year VLBI monitoring program (2005–2009) at 22 and 43 GHz recently published by Baczkó et al. (2019) reveals large amplitude variations of about 1.8 Jy (78%) and 1.2 Jy (70%), respectively, for the total nuclear emission (see Table A1), which can account for the apparent bump seen in the high-angular resolution data at radio wavelengths (Fig. 7). Optical depth effects can seriously affect the continuum shape in this range, thus we keep a simple power law in our fit since capturing the complex distribution of the optically-thick components in the jet is beyond the scope of this paper. A combination of IR dust and radio synchrotron emission can also explain the overall flux distribution of radio galaxies (e.g. Müller et al. 2004; Lopez-Rodriguez et al. 2018b). However in the case of NGC 1052 the VLBI radio core, which suffers from heavy free-free absorption below $\lesssim 43$ GHz (Kadler et al. 2004), becomes the dominant nuclear contribution ($\sim 70\%$ of total flux) at 86 GHz (Tables A1 and A2; Baczkó et al. 2016). This flux is confined within the innermost $0.407 \times 0.075\ \text{mas}^2$ region (42.3×7.8 light days 2), that is of the order of the R_{in} estimated in Section 3.2, suggesting that most of millimetre/submillimetre emission comes from the vicinity of the black hole¹¹. The ALMA archival observations at 478 GHz presented in this work, with an angular resolution of $0''.12 \times 0''.10$ ($10 \times 9\ \text{pc}^2$), do not show any extended structure in the millimetre/submillimetre range that could be indicative of extended cold dust emission from

¹¹ $\sim 450\text{--}2400\ R_S$ in Schwarzschild radii for $M_{\text{BH}} = 1.55 \times 10^8 M_\odot$.

the torus. This is further confirmed by recent band 7 observations at 65×53 mas resolution (5.7×4.6 pc; Kamenov et al. priv. comm.). On the contrary, the ALMA fluxes included in Table A1 are in good agreement with large aperture measurements in Table A2. Future continuum ALMA observations at sub-parsec resolution ($\lesssim 0''.01$) at higher frequencies ($\gtrsim 600$ GHz) would be useful to probe the possible contribution of thermal cold dust emission. Besides the compact emission, the existence of an extended jet at radio wavelengths is well known on both arcsecond (Wrobel 1984; Cooper et al. 2007) and milliarcsecond scales (Claussen et al. 1998; Baczkowski et al. 2019).

Regarding the polarisation, a compact jet does not require any extinction to explain the degree of linear polarisation measured in this work. The difference in the polarisation angle between the near- and the mid-IR measurements ($\sim 50^\circ$; Table 2) suggests that multiple jet components might be included within the inner few tens of parsecs. This is the case of M87, where abrupt changes of $\sim 90^\circ$ have been found between contiguous regions resolved along the jet, likely driven by the helical structure of the magnetic field (Avachat et al. 2016). Since the relative contribution of these components to the total flux varies with wavelength – for instance HST-1 outshines the core in the UV at certain epochs – changes in the PA of the integrated polarised flux between different filters are not surprising.

As mentioned in Section 4.1, the analysis of *Swift* observations revealed a “harder when brighter” variability behaviour in the X-rays (Connolly et al. 2016), as opposed to the “softer when brighter” behaviour shown by Seyfert galaxies (e.g. Caballero-Garcia et al. 2012, Peretz & Behar 2018). This is hard to explain in terms of a variable column gas density, since a harder X-ray slope produced by an increasing N_{H} should be followed by a drop in the observed flux. However, the opposite behaviour is a well known characteristic of X-ray binaries in the hard state. This is ascribed to the recession of the disc and the transition to an advection-dominated flow at low accretion rates (Narayan et al. 1995). At this point the self-Comptonisation of synchrotron photons radiated by the corona and/or the jet becomes the dominant contribution in the X-rays. This mechanism applies also to blazars, where the injection of highly energetic electrons in the jet, e.g. due to a shock re-acceleration or a magnetic re-connection event, increases both the overall luminosity and the peak frequency of the inverse Compton component (10 MeV–100 GeV), steepening the observed X-ray spectral slope (e.g. Ghisellini et al. 2009, Wang et al. 2018). A similar trend has also been observed in the LINER nucleus of NGC 7213 (Emmanoulopoulos et al. 2012). In this context, we interpret the $N_{\text{H}} \sim 10^{23} \text{ cm}^{-2}$ column density as a dense neutral and/or ionised gas absorber in the innermost nuclear region, but not associated with a dusty medium. This is in line with the detection of broad lines in both the polarised and the total intensity spectra. Additionally, NGC 1052 fits in the correlation found by Koljonen et al. (2015) between the X-ray power-law index and the turnover frequency found at IR-to-radio wavelengths also followed by X-ray binaries, suggesting that the properties of both the plasma close to the black hole and the accelerated particles in the jet are tightly related.

A drawback of the jet scenario is that a larger variability would be expected in the IR-to-UV continuum. So far, NGC 1052 have shown a consistent mid-IR flux over six different epochs in the 2007–2015 period, including VISIR, T-ReCS, and CanariCam, while tentative UV variability was reported by Maoz et al. (2005). In the millimetre range, the core displays a fairly stable flux with occasional burst (two in the 1972–1981 period; Heeschen & Conklin 1975). Thus, NGC 1052 seems to be a relatively stable source during most of the time. A monitoring campaign in the UV range

would be required in order to probe the variability associated with the most energetic particles in the jet framework.

While compact jet emission in the IR-to-optical continuum has been suggested for active nuclei in the past (e.g. M81 in Markoff et al. 2008, NGC 4151 in Maitra et al. 2011), NGC 1052 is the first LLAGN where this component has been first identified by its characteristic continuum spectral shape, and then isolated in the mid-IR range at milliarcsecond resolution. The synchrotron core of Centaurus A was studied using MIDI interferometry by Meisenheimer et al. (2007) and Burtscher et al. (2010). However, in this case the shape of the continuum emission is seriously affected by the high foreground extinction ($A_{\text{V}} \sim 14$ mag), which hampers the identification of the power-law flux distribution in the optical/UV range.

Previous studies combining RIAF and jet models have been used to fit the continuum emission in LLAGN, but these efforts have not been conclusive on the nature of the UV-to-IR continuum, while the case of NGC 1052 remains hard to reproduce by these models (see Yuan et al. 2009; Yu et al. 2011). This is likely due to the prominent slope in the IR-to-UV range, which departs largely from the canonical optically-thin spectral index assumed in these models ($\alpha \sim 0.7$), thus RIAF plus standard jet models have serious problems to accommodate such a steep continuum. In this regard, steep optical spectra with $\alpha \sim 2$ have been found to be common among LLAGN (Ho et al. 1996; Ho 1999). In the context of accelerated particles in a jet, a spectral index of $\alpha \gtrsim 2.6$ corresponds to an index of $p \gtrsim 6.2$ in the energy distribution of the accelerated particles [$N(E)dE \propto E^{-p} dE$], which would imply an extremely efficient – and possibly unphysical – cooling process. Even if we adopt an extinction of $A_{\text{V}} = 1.05$ mag (Dopita et al. 2015), the corrected spectral index would be $\alpha = 2.2$ ($p = 5.4$; grey circles in Fig. 7). Thus, we favour a thermalised energy distribution for the radiating particles as a more likely scenario to explain the steepness of the continuum distribution. This could be associated with particles in the corona or the base of the jet that have not been shocked, and therefore do not follow a power-law energy distribution, a scenario that has also been suggested in X-ray binaries (e.g. Jones & Hardee 1979; Gallo et al. 2007; Russell et al. 2010; Shahbaz et al. 2013; Reb et al. 2018).

A continuum distribution as that shown by NGC 1052 is 0.3 dex above¹² the mid-IR – X-ray correlation derived by Asmus et al. (2015), i.e. over-luminous in the mid-IR although still within the intrinsic scatter. Note that the compact jet scenario would also imply a correlation between IR and X-ray fluxes, since the X-ray emission would rely on the Comptonisation of available IR-to-UV seed photons produced by the jet. The flux distribution shows also a $2500 \text{ \AA} - 2 \text{ keV}$ spectral index¹³ in agreement with brighter nuclei dominated by a prominent accretion disc (Maoz 2007). This means that *NGC 1052 alike nuclei are able to mimic the values typically associated with the presence of tori and accretion discs, despite the lack of a thermal continuum signature in the flux distribution.* The steep continuum explains the elusive nature of the nuclear emission in the IR-to-optical range for NGC 1052, a characteristic likely extensible to a number of objects that belong to the LLAGN class (e.g. NGC 1097, M87, Sombrero Galaxy in Koljonen et al. 2015). The existence of a truncated accretion disc is suggested by

¹² For an intrinsic X-ray luminosity of $\log(L_{2-10\text{keV}}/\text{erg s}^{-1}) = 41.45 \pm 0.08$, a mid-IR luminosity of $\log(L_{12\mu\text{m}}/\text{erg s}^{-1}) \sim 41.83$, compared to the $\log(L_{12\mu\text{m}}/\text{erg s}^{-1}) = 42.12 \pm 0.06$ measured for NGC 1052.

¹³ $\alpha_{\text{ox}} \sim -0.6$, derived from the high-angular resolution measurements in Table A1.

the detection of a broad Fe K α line at 6.4 keV (Brenneman et al. 2009), while the presence of warm dust is indicated by the 9.7 μ m silicate emission (Fig. 2). Nevertheless, their net contribution to the overall continuum emission in NGC 1052 appears to be negligible, as self-Compton synchrotron emission from a compact jet seems to dominate the energy output across the whole electromagnetic spectrum, that is over eleven orders of magnitude in frequency.

5 SUMMARY

In this work we acquired *N*-band interferometric observations with VLTI/MIDI to investigate the nature of the mid-IR emission in one of the few LLAGN that can be observed using this technique, the prototypical LINER nucleus in NGC 1052. Additionally, we measure the degree and position angle of the linear polarisation in the near-to mid-IR continuum, using WHT/LIRIS and GTC/CanariCam. With MIDI we found an unresolved nucleus (< 5 mas ~ 0.5 pc) up to the longest baselines available to the UTs (~ 130 m; Section 3). We explored two main scenarios for the unresolved emission: an exceptionally compact dust distribution and a compact jet. After a detailed analysis we favour the latter scenario (Section 4.2), which is further supported by several points of evidence: *i*) the broken power-law shape shown by the continuum spectral distribution from radio to UV wavelengths; *ii*) a $\sim 4\%$ degree of polarisation measured in mid-IR range, together with a low extinction along the line of sight ($A_V \sim 1$ mag); *iii*) the “harder when brighter” behaviour in the X-rays indicative of self-Compton synchrotron radiation, a known property of X-ray binaries in the hard state and blazars. Alternatively, if the mid-IR core is dominated by thermal dust emission, this would require first an exceptionally compact dust distribution when compared to those measured in nearby AGN (e.g. Circinus, see Section 4.1), and second an extinction of $A_V \sim 26$ mag (2.8 mag assuming the maximum efficiency for the dichroic mechanism). The latter is in contrast with several observational facts: the $A_V \sim 1$ mag determined from *HST*/FOS observations, the well defined power-law shape of the IR-to-UV continuum, the detection of the silicate band in emission for a highly inclined system, the presence of broad H α and H β lines in the unpolarised spectrum, and the increasing hardness at X-rays (higher N_H) with increasing luminosity.

A distinctive characteristic of NGC 1052 when compared to jets in classical radio galaxies is the steepness of the power-law continuum in the IR-to-UV range ($\alpha \sim 2.6$). However such a steep distribution could be common among LLAGN, as suggested by the steep ($\alpha \sim 2$) optical/UV power-law continuum observed in LINERs. A similar behaviour has been reported also for X-ray binaries in the low/hard state. The steep IR-to-UV continuum explains the elusive nature of NGC 1052 – and possibly a number of LLAGN – at optical wavelengths. Furthermore, despite the lack of a thermal continuum in the flux distribution, NGC 1052 does not depart largely from the mid-IR – X-ray correlation, and also mimics the UV – X-ray ratios of brighter nuclei. This behaviour is usually driven by a continuum emission dominated by the torus and the accretion disc, respectively. No significant IR variability has been detected for this nucleus over the 2007–2015 period, although a monitoring campaign in the UV would be required to probe the synchrotron radiation variability at the highest energies, also searching for possible occasional bursts as those reported in the millimetre range by Heeschen & Puschell (1983).

The combination of multi-wavelength analysis, polarimetric, and interferometric observations used in this work offers a unique approach to investigate the nature of the nuclear continuum emission

in nearby galaxies. The case of NGC 1052 suggests that compact jets might be common at the heart of several LLAGN. Future high-angular resolution observations of LLAGN with the *James Webb Space Telescope* (*JWST*) and the Extreme Large Telescopes (ELTs) will be crucial to shed light on the nature of the continuum radiation in these nuclei.

ACKNOWLEDGEMENTS

The authors acknowledge the referee for his/her useful comments that helped to improve the manuscript. This study is based on observations collected at the European Southern Observatory, Chile, programmes 093.B-0616, 094.B-0918, 086.B-0349, 095.B-0376. The following ALMA data has also been used in this work: ADS/JAO.ALMA#2013.1.00749.S. ALMA is a partnership of ESO (representing its member states), NSF (USA) and NINS (Japan), together with NRC (Canada), MOST and ASIAA (Taiwan), and KASI (Republic of Korea), in cooperation with the Republic of Chile. The Joint ALMA Observatory is operated by ESO, AUI/NRAO and NAOJ. This research has made use of *ASTROPY*¹⁴, a community-developed core PYTHON package for Astronomy (*Astropy Collaboration et al.* 2013, 2018), and the NASA/IPAC Infrared Science Archive, which is operated by the Jet Propulsion Laboratory, California Institute of Technology, under contract with the National Aeronautics and Space Administration.

JAFO and MAP acknowledge financial support from the Spanish Ministry of Economy under grant number MEC-AYA2015-53753-P. The research leading to these results has received funding from the European Union’s Horizon 2020 research and innovation programme under Grant Agreement 730890 (OPTICON). DA acknowledges support from the European Union’s Horizon 2020 Innovation programme under the Marie Skłodowska-Curie grant agreement no. 793499 (DUSTDEVILS).

References

- Ajello M., et al., 2009, *ApJ*, 699, 603
- Alves F. O., Acosta-Pulido J. A., Girat J. M., Franco G. A. P., López R., 2011, *AJ*, 142, 33
- Antonucci R., 1993, *ARA&A*, 31, 473
- Asmus D., Hönig S. F., Gandhi P., Smette A., Duschl W. J., 2014, *MNRAS*, 439, 1648
- Asmus D., Gandhi P., Hönig S. F., Smette A., Duschl W. J., 2015, *MNRAS*, 454, 766
- Astropy Collaboration et al., 2013, *A&A*, 558, A33
- Astropy Collaboration et al., 2018, *AJ*, 156, 123
- Avachat S. S., Perlman E. S., Adams S. C., Cara M., Owen F., Sparks W. B., Georganopoulos M., 2016, *ApJ*, 832, 3
- Baczko A.-K., et al., 2016, *A&A*, 593, A47
- Baczko A. K., Schulz R., Kadler M., Ros E., Perucho M., Fromm C. M., Wilms J., 2019, arXiv e-prints, p. arXiv:1901.02639
- Bagri D. S., Ananthakrishnan S., 1984, in *VLBI and Compact Radio Sources*. Symposium no. 110 held in Bologna, Italy, June 27–July 1, 1983. Edited by R. Fanti, K. Kellermann, and G. Setti. p.261, 1984. p. 261
- Barth A. J., Filippenko A. V., Moran E. C., 1999, *ApJ*, 525, 673
- Barvainis R., 1987, *ApJ*, 320, 537
- Becklin E. E., Tokunaga A. T., Wynn-Williams C. G., 1982, *ApJ*, 263, 624
- Beckmann V., et al., 2009, *A&A*, 505, 417
- Blandford R. D., Königl A., 1979, *ApJ*, 232, 34

¹⁴ <http://www.astropy.org>

- Brenneman L. W., et al., 2009, *ApJ*, 698, 528
- Bressan A., et al., 2006, *ApJ*, 639, L55
- Burtscher L., Meisenheimer K., Jaffe W., Tristram K. R. W., Röttgering H. J. A., 2010, *Publ. Astron. Soc. Australia*, 27, 490
- Burtscher L., Tristram K. R. W., Jaffe W. J., Meisenheimer K., 2012, in *Optical and Infrared Interferometry III*. p. 84451G (arXiv:1206.6620), doi:10.1117/12.925521
- Burtscher L., et al., 2013, *A&A*, 558, A149
- Caballero-Garcia M. D., Papadakis I. E., Nicastro F., Ajello M., 2012, *A&A*, 537, A87
- Cardelli J. A., Clayton G. C., Mathis J. S., 1989, *ApJ*, 345, 245
- Claussen M. J., Diamond P. J., Braatz J. A., Wilson A. S., Henkel C., 1998, *ApJ*, 500, L129
- Cohen M., Walker R. G., Carter B., Hammersley P., Kidger M., Noguchi K., 1999, *AJ*, 117, 1864
- Cohen A. S., Lane W. M., Cotton W. D., Kassim N. E., Lazio T. J. W., Perley R. A., Condon J. J., Erickson W. C., 2007, *AJ*, 134, 1245
- Condon J. J., Dressel L. L., 1978, *ApJ*, 221, 456
- Connolly S. D., McHardy I. M., Skipper C. J., Emmanoulopoulos D., 2016, *MNRAS*, 459, 3963
- Cooper N. J., Lister M. L., Kochanzyk M. D., 2007, *ApJS*, 171, 376
- Cusumano G., et al., 2010, *A&A*, 524
- Di Matteo T., Allen S. W., Fabian A. C., Wilson A. S., Young A. J., 2003, *ApJ*, 582, 133
- Dopita M. A., et al., 2015, *ApJ*, 801, 42
- Douglas J. N., Bash F. N., Bozyan F. A., Torrence G. W., Wolfe C., 1996, *AJ*, 111, 1945
- Elitzur M., Ho L. C., 2009, *ApJ*, 701, L91
- Elitzur M., Shlosman I., 2006, *ApJ*, 648, L101
- Elvis M., et al., 1994, *The Astrophysical Journal Supplement Series*, 95, 1
- Emmanoulopoulos D., Papadakis I. E., McHardy I. M., Arévalo P., Calvelo D. E., Uttley P., 2012, *MNRAS*, 424, 1327
- Fabian A. C., Rees M. J., 1995, *MNRAS*, 277, L55
- Fernández-Ontiveros J. A., Prieto M. A., Acosta-Pulido J. A., Montes M., 2012, in *Journal of Physics Conference Series*. p. 012006 (arXiv:1206.0777), doi:10.1088/1742-6596/372/1/012006
- Fernández-Ontiveros J. A., Tristram K. R. W., Hönic S., Gandhi P., Weigelt G., 2018, *A&A*, 611
- Fey A. L., Charlot P., 1997, *ApJS*, 111, 95
- Filippenko A. V., 1985, *ApJ*, 289, 475
- Fosbury R. A. E., Mebold U., Goss W. M., Dopita M. A., 1978, *MNRAS*, 183, 549
- Gallo E., Migliari S., Markoff S., Tomsick J. A., Bailyn C. D., Berta S., Fender R., Miller-Jones J. C. A., 2007, *ApJ*, 670, 600
- Ghisellini G., Maraschi L., Tavecchio F., 2009, *MNRAS*, 396, L105
- González-Martín O., Masegosa J., Márquez I., Guainazzi M., Jiménez-Bailón E., 2009, *A&A*, 506, 1107
- Greenhill L. J., et al., 2003, *ApJ*, 590, 162
- Hatziminaoglou E., Hernán-Caballero A., Feltre A., Piñol Ferrer N., 2015, *ApJ*, 803, 110
- Heckman T. M., 1980, *A&A*, 87, 152
- Heeschen D. S., 1973, *ApJ*, 179, L93
- Heeschen D. S., Conklin E. K., 1975, *ApJ*, 196, 347
- Heeschen D. S., Puschell J. J., 1983, *ApJ*, 267, L11
- Hernández-García L., González-Martín O., Masegosa J., Márquez I., 2014, *A&A*, 569
- Ho L. C., 1999, *ApJ*, 516, 672
- Ho L. C., 2008, *ARA&A*, 46, 475
- Ho L. C., Filippenko A. V., Sargent W. L. W., 1996, *ApJ*, 462, 183
- Ho L. C., Filippenko A. V., Sargent W. L. W., 1997, *ApJS*, 112, 315
- Ho L. C., et al., 2001, *ApJ*, 549, L51
- Hönig S. F., Beckert T., 2007, *MNRAS*, 380, 1172
- Hönig S. F., Kishimoto M., Gandhi P., Smette A., Asmus D., Duschl W., Polletta M., Weigelt G., 2010, *A&A*, 515, A23
- Jaffe W. J., 2004, in Traub W. A., ed., *Society of Photo-Optical Instrumentation Engineers (SPIE) Conference Series Vol. 5491*, Society of Photo-Optical Instrumentation Engineers (SPIE) Conference Series. p. 715
- Jensen J. B., Tonry J. L., Barris B. J., Thompson R. I., Liu M. C., Rieke M. J., Ajhar E. A., Blakeslee J. P., 2003, *ApJ*, 583, 712
- Jones T. J., 1989, *ApJ*, 346, 728
- Jones T. W., Hardee P. E., 1979, *ApJ*, 228, 268
- Kadler M., Ros E., Lobanov A. P., Falcke H., Zensus J. A., 2004, *A&A*, 426, 481
- Kameno S., Sawada-Satoh S., Inoue M., Shen Z.-Q., Wajima K., 2001, *PASJ*, 53, 169
- Kaneda H., Onaka T., Sakon I., Kitayama T., Okada Y., Suzuki T., 2008, *ApJ*, 684, 270
- Käuff H. U., et al., 2015, *The Messenger*, 159, 15
- Keating S. K., Everett J. E., Gallagher S. C., Deo R. P., 2012, *ApJ*, 749, 32
- Keel W. C., Miller J. S., 1983, *ApJ*, 266, L89
- Kerber F., et al., 2016, in *Ground-based and Airborne Instrumentation for Astronomy VI*. p. 99080D, doi:10.1117/12.2232441
- Kishimoto M., Hönic S. F., Beckert T., Weigelt G., 2007, *A&A*, 476, 713
- Kishimoto M., Hönic S. F., Tristram K. R. W., Weigelt G., 2009, *A&A*, 493, L57
- Kishimoto M., Hönic S. F., Antonucci R., Millour F., Tristram K. R. W., Weigelt G., 2011, *A&A*, 536, A78
- Knapp G. R., Patten B. M., 1991, *AJ*, 101, 1609
- Koljonen K. I. I., et al., 2015, *ApJ*, 814, 139
- Koski A. T., Osterbrock D. E., 1976, *ApJ*, 203, L49
- Lagage P. O., et al., 2004, *The Messenger*, 117, 12
- Large M. I., Mills B. Y., Little A. G., Crawford D. F., Sutton J. M., 1981, *MNRAS*, 194, 693
- Lebouteiller V., Barry D. J., Goes C., Sloan G. C., Spoon H. W. W., Weedman D. W., Bernard-Salas J., Houck J. R., 2015, *ApJS*, 218, 21
- Leinert C., et al., 2003, *Ap&SS*, 286, 73
- Lenzen R., et al., 2003, in Iye M., Moorwood A. F. M., eds, *Proc. SPIE Vol. 4841, Instrument Design and Performance for Optical/Infrared Ground-based Telescopes*. pp 944–952, doi:10.1117/12.460044
- López-Gonzaga N., Jaffe W., Burtscher L., Tristram K. R. W., Meisenheimer K., 2014, *A&A*, 565
- Lopez-Rodriguez E., et al., 2016, *MNRAS*, 458, 3851
- Lopez-Rodriguez E., et al., 2018a, *MNRAS*, 478, 2350
- Lopez-Rodriguez E., Antonucci R., Chary R.-R., Kishimoto M., 2018b, *ApJ*, 861, L23
- Maitra D., Miller J. M., Markoff S., King A., 2011, *ApJ*, 735, 107
- Maoz D., 2007, *MNRAS*, 377, 1696
- Maoz D., Nagar N. M., Falcke H., Wilson A. S., 2005, *ApJ*, 625, 699
- Marchese E., Della Ceca R., Caccianiga A., Severgnini P., Corral A., Fanali R., 2012, *A&A*, 539, A48
- Marino A., et al., 2011, *MNRAS*, 411, 311
- Markoff S., Nowak M. A., Wilms J., 2005, *ApJ*, 635, 1203
- Markoff S., et al., 2008, *ApJ*, 681
- Marscher A. P., 2014, *ApJ*, 780, 87
- Marscher A. P., et al., 2008, *Nature*, 452, 966
- Mason R. E., et al., 2012, *AJ*, 144
- Mason R. E., Ramos Almeida C., Levenson N. A., Nemmen R., Alonso-Herrero A., 2013, *ApJ*, 777
- Meisenheimer K., et al., 2007, *A&A*, 471, 453
- Müller S. A. H., Haas M., Siebenmorgen R., Klaas U., Meisenheimer K., Chini R., Albrecht M., 2004, *A&A*, 426, L29
- Naghizadeh-Khouei J., Clarke D., 1993, *A&A*, 274, 968
- Narayan R., Yi I., Mahadevan R., 1995, *Nature*, 374, 623
- Nemmen R. S., Storchi-Bergmann T., Eracleous M., 2014, *MNRAS*, 438, 2804
- Nicastro F., Martocchia A., Matt G., 2003, *ApJ*, 589, L13
- O’Connell R. W., Dressel L. L., 1978, *Nature*, 276, 374
- Oliva E., 1997, *Astronomy and Astrophysics Supplement Series*, 123, 589
- Pacholczyk A. G., 1970, *Radio astrophysics. Nonthermal processes in galactic and extragalactic sources*. W.H.Freeman & Co Ltd.
- Pasetto A., González-Martín O., Esparza- Arredondo D., Osorio-Clavijo N., Victoria- Ceballos C., Martínez-Paredes M., 2019, arXiv e-prints, p. arXiv:1901.02280
- Peretz U., Behar E., 2018, *MNRAS*, 481, 3563
- Polko P., Meier D. L., Markoff S., 2014, *MNRAS*, 438, 959

- Prieto M. A., Fernández-Ontiveros J. A., Markoff S., Espada D., González-Martín O., 2016, *MNRAS*, 457, 3801
- Ramírez E. A., Tadhunter C. N., Axon D., Batcheldor D., Packham C., Lopez-Rodríguez E., Sparks W., Young S., 2014, *MNRAS*, 444, 466
- Reb L., Fernández-Ontiveros J. A., Prieto M. A., Dolag K., 2018, *MNRAS*, 478, L122
- Ricci R., Prandoni I., Gruppioni C., Sault R. J., de Zotti G., 2006, *A&A*, 445, 465
- Rieke G. H., Lebofsky M. J., Kemp J. C., 1982, *ApJ*, 252, L53
- Rousset G., et al., 2003, in Wizinowich P. L., Bonaccini D., eds, *Proc. SPIE Vol. 4839, Adaptive Optical System Technologies II*. pp 140–149, doi:10.1117/12.459332
- Russell D. M., Maitra D., Dunn R. J. H., Markoff S., 2010, *MNRAS*, 405, 1759
- Sawada-Satoh S., et al., 2016, *ApJ*, 830
- Schlafly E. F., Finkbeiner D. P., 2011, *ApJ*, 737, 103
- Schmidt G. D., Elston R., Lupie O. L., 1992, *AJ*, 104, 1563
- Serkowski K., Mathewson D. S., Ford V. L., 1975, *ApJ*, 196, 261
- Shaffer D. B., Marscher A. P., 1979, *ApJ*, 233, L105
- Shahbaz T., Russell D. M., Zurita C., Casares J., Corral-Santana J. M., Dhillon V. S., Marsh T. R., 2013, *MNRAS*, 434, 2696
- Strom S. E., Vrba F. J., Strom K. M., 1976, *AJ*, 81, 314
- Sugai H., Malkan M. A., 2000, *ApJ*, 529, 219
- Sugai H., et al., 2005, *ApJ*, 629, 131
- Suganuma M., et al., 2006, *ApJ*, 639, 46
- Tamura M., Yamashita T., Sato S., Nagata T., Gatley I., 1988, *MNRAS*, 231, 445
- Telesco C. M., et al., 2003, in Iye M., Moorwood A. F. M., eds, *Society of Photo-Optical Instrumentation Engineers (SPIE) Conference Series Vol. 4841, Instrument Design and Performance for Optical/Infrared Ground-based Telescopes*. pp 913–922, doi:10.1117/12.458979
- Terashima Y., Wilson A. S., 2003, *ApJ*, 583, 145
- Terlevich R., Melnick J., 1985, *MNRAS*, 213, 841
- Tingay S. J., Jauncey D. L., King E. A., Tzioumis A. K., Lovell J. E. J., Edwards P. G., 2003, *PASJ*, 55, 351
- Torniainen I., Tornikoski M., Lähteenmäki A., Aller M. F., Aller H. D., Mingaliev M. G., 2007, *A&A*, 469, 451
- Tristram K. R. W., Schartmann M., 2011, *A&A*, 531, A99
- Tristram K. R. W., et al., 2009, *A&A*, 502, 67
- Tristram K. R. W., Burtscher L., Jaffe W., Meisenheimer K., Hönig S. F., Kishimoto M., Schartmann M., Weigelt G., 2014, *A&A*, 563, A82
- Tueller J., et al., 2010, *ApJS*, 186, 378
- Urry C. M., Padovani P., 1995, *PASP*, 107, 803
- Wang Y., Xue Y., Zhu S., Fan J., 2018, *ApJ*, 867, 68
- Whittet D. C. B., 1996, in Roberge W. G., Whittet D. C. B., eds, *Astronomical Society of the Pacific Conference Series Vol. 97, Polarimetry of the Interstellar Medium*. p. 125
- Whittet D. C. B., Martin P. G., Hough J. H., Rouse M. F., Bailey J. A., Axon D. J., 1992, *ApJ*, 386, 562
- Woo J.-H., Urry C. M., 2002, *ApJ*, 579, 530
- Wrobel J. M., 1984, *ApJ*, 284, 531
- Yu Z., Yuan F., Ho L. C., 2011, *ApJ*, 726, 87
- Yuan F., Yu Z., Ho L. C., 2009, *ApJ*, 703, 1034
- Zschaechner L. K., et al., 2016, *ApJ*, 832, 142

This paper has been typeset from a $\text{\TeX}/\text{\LaTeX}$ file prepared by the author.

APPENDIX A: THE SPECTRAL FLUX DISTRIBUTION OF NGC 1052

Table A1. Spectral flux distribution for the nucleus of NGC 1052 at subarcsec aperture resolution flux. Tabulated values have not been corrected for Galactic reddening. Intrinsic X-ray fluxes are derived from apertures of a few to several arcseconds in size, however the host galaxy contribution in this range is negligible, thus the fluxes are assumed as representative from the nuclear source. The asterisk symbol in the flux column denotes the presence of multiple jet components resolved within the inner 0".15 in the 2.3–89 GHz range. In this case the tabulated fluxes correspond to the sum of all the jet components.

Frequency [Hz]	F_{ν} [Jy]	Aperture [radius/beam]	Telescope/Band	Reference
2.53×10^{19}	$(1.5 \pm 0.3) \times 10^{-7}$		<i>Swift</i> /BAT, 14–195 keV	Tueller et al. 2010
1.99×10^{19}	$(1.4 \pm 0.8) \times 10^{-7}$		<i>Swift</i> /BAT, 15–150 keV	Cusumano et al. 2010
1.6926×10^{19}	1.1×10^{-7}		<i>INTEGRAL</i> , 40–100 keV	Beckmann et al. 2009
8.463×10^{18}	3.0×10^{-7}		<i>Suzaku</i> , 10–60 keV	Brenneman et al. 2009
8.463×10^{18}	$(1.6 \pm 0.2) \times 10^{-7}$		<i>Swift</i> /BAT, 15–55 keV	Ajello et al. 2009
7.254×10^{18}	1.7×10^{-7}		<i>INTEGRAL</i> , 20–40 keV	Beckmann et al. 2009
1.4508×10^{18}	$2.9^{+0.75}_{-2.44} \times 10^{-7}$		<i>Chandra</i> , 2–10 keV	González-Martín et al. 2009
1.4508×10^{18}	4.6×10^{-7}		<i>Suzaku</i> , 2–10 keV	Brenneman et al. 2009
1.1046×10^{15}	$(8.1 \pm 0.3) \times 10^{-6}$	0".15	<i>HST</i> /ACS-HRC, F250W	This work
8.9206×10^{14}	$(1.48 \pm 0.03) \times 10^{-5}$	0".15	<i>HST</i> /ACS-HRC, F330W	This work
5.5006×10^{14}	$(3.4 \pm 0.1) \times 10^{-5}$	0".15	<i>HST</i> /WFPC1, F555W	This work
2.3715×10^{14}	$(6.3 \pm 0.1) \times 10^{-4}$	0".26	VLT/NaCo, J band	This work
1.868×10^{14}	$(8.0 \pm 0.3) \times 10^{-4}$	0".15	<i>HST</i> /NIC2, F160W	This work
1.3761×10^{14}	$(1.19 \pm 0.02) \times 10^{-3}$	0".15	VLT/NaCo, Ks band	This work
7.8947×10^{13}	$(7.17 \pm 0.03) \times 10^{-3}$	0".15	VLT/NaCo, L' band	This work
3.86×10^{13}	$(58.8 \pm 9.4) \times 10^{-3}$	0".52 × 0".39	VLT/VISIR, J7.9	Asmus et al. 2014
3.49×10^{13}	$(62.4 \pm 14.4) \times 10^{-3}$	0".45 × 0".39	VLT/VISIR, PAH1	Asmus et al. 2014
3.49×10^{13}	$(58 \pm 14) \times 10^{-3}$	0".45 × 0".40	VLT/VISIR, PAH1	This work
3.446×10^{13}	$(63 \pm 6) \times 10^{-3}$	0".5	GTC/CanariCam, Si2	This Work
3.43×10^{13}	$(63.6 \pm 1.6) \times 10^{-3}$	0".75 × 0".62	Gemini/T-ReCS, Si2	Asmus et al. 2014
3.05×10^{13}	$(114.7 \pm 22.9) \times 10^{-3}$	0".39 × 0".35	VLT/VISIR, B9.7	Asmus et al. 2014
2.81×10^{13}	$(133.7 \pm 22.8) \times 10^{-3}$	0".43 × 0".37	VLT/VISIR, B10.7	Asmus et al. 2014
2.6×10^{13}	$(154.1 \pm 13.2) \times 10^{-3}$	0".44 × 0".40	VLT/VISIR, B11.7	Asmus et al. 2014
2.584×10^{13}	$(123 \pm 12) \times 10^{-3}$	0".5	GTC/CanariCam, Si5	This Work
2.52×10^{13}	$(133.9 \pm 4.2) \times 10^{-3}$	0".40 × 0".36	VLT/VISIR, PAH2_2	Asmus et al. 2014
2.52×10^{13}	$(133 \pm 4) \times 10^{-3}$	0".40 × 0".40	VLT/VISIR, PAH2_2	This work
2.4×10^{13}	$(181.2 \pm 19.8) \times 10^{-3}$	0".51 × 0".42	VLT/VISIR, B12.4	Asmus et al. 2014
1.64×10^{13}	$(355.7 \pm 9.1) \times 10^{-3}$	0".55 × 0".52	Gemini/T-ReCS, Qa	Asmus et al. 2014
1.6×10^{13}	$(339.0 \pm 33.8) \times 10^{-3}$	0".50 × 0".49	VLT/VISIR, Q2	Asmus et al. 2014
4.778×10^{11}	$(201 \pm 2) \times 10^{-3}$	0".12 × 0".10	ALMA, 478 GHz	This work
4.657×10^{11}	$(207 \pm 1) \times 10^{-3}$	0".12 × 0".10	ALMA, 466 GHz	This work
4.315×10^{11}	$(273 \pm 1) \times 10^{-3}$	0".13 × 0".12	ALMA, 432 GHz	This work
4.194×10^{11}	$(283 \pm 1) \times 10^{-3}$	0".14 × 0".12	ALMA, 419 GHz	This work
3.528×10^{11}	$(283.1 \pm 1.1) \times 10^{-3}$	0".20 × 0".15	ALMA, 353 GHz	Pasetto et al. 2019
3.408×10^{11}	$(299.3 \pm 1.1) \times 10^{-3}$	0".20 × 0".15	ALMA, 341 GHz	Pasetto et al. 2019
2.294×10^{11}	$(457 \pm 4) \times 10^{-3}$	0".3 × 0".2	ALMA, 229 GHz	Pasetto et al. 2019
2.141×10^{11}	$(495 \pm 3) \times 10^{-3}$	0".3 × 0".2	ALMA, 214 GHz	Pasetto et al. 2019
1.080×10^{11}	$(750 \pm 7) \times 10^{-3}$	0".7 × 0".6	ALMA, 108 GHz	Pasetto et al. 2019
8.9×10^{10}	0.561*	$1.44 \times 0.90 \text{ mas}^2$	KVN, 89 GHz	Sawada-Satoh et al. 2016
8.6×10^{10}	$0.62 \pm 0.09^*$	$0.407 \times 0.075 \text{ mas}^2$	GMVA, 86 GHz	Baczko et al. 2016
4.3×10^{10}	0.49–1.64	$1.11 \times 0.21 \text{ mas}^2$	VLBI, 43 GHz, min–max 2005–2009	Baczko et al. 2019
2.21×10^{10}	2.46 ± 0.02	0".09 × 0".07	JVLA, 22 GHz	Pasetto et al. 2019
2.2×10^{10}	0.50–2.26	$0.96 \times 0.37 \text{ mas}^2$	VLBI, 22 GHz, min–max 2005–2009	Baczko et al. 2019
1.5364×10^{10}	$1.99 \pm 0.04^*$	$1.03 \times 0.40 \text{ mas}^2$	VLBA, 15 GHz	Kameno et al. 2001
1.49×10^{10}	1.0 ± 0.1	0".1 × 0".09	JVLA, 15 GHz	Pasetto et al. 2019
8.4×10^9	2.91 ± 0.03	0".3 × 0".2	JVLA, 8.4 GHz	Pasetto et al. 2019
8.4×10^9	2.39*	$1.98 \times 0.81 \text{ mas}^2$	VLBI, 8.4 GHz	Kadler et al. 2004
6.2×10^9	1.295 ± 0.001	0".4 × 0".3	JVLA, 6.2 GHz	Pasetto et al. 2019
5.0×10^9	2.41*	$3.3 \times 1.31 \text{ mas}^2$	VLBI, 5 GHz	Kadler et al. 2004
2.32×10^9	1.51*	$9.0 \times 3.8 \text{ mas}^2$	VLBA, 2.3 GHz	Fey & Charlot 1997
1.6710×10^9	0.62 ± 0.06	3.40 mas	VLBI, 1.7 GHz	Shaffer & Marscher 1979
3.27×10^8	0.30 ± 0.15	0".1	Ooty Radio Telescope, 327 MHz	Bagri & Ananthakrishnan 1984

Table A2. Spectral flux distribution for the nucleus of NGC 1052 extracted from large aperture ($\gtrsim 1''$) flux measurements.

Frequency [Hz]	F_ν [Jy]	Aperture [radius/beam]	Telescope/Band	Reference
1.95×10^{15}	$(7.7 \pm 0.6) \times 10^{-5}$	4''21	GALEX FUV	Marino et al. 2011
1.29×10^{15}	$(1.47 \pm 0.06) \times 10^{-4}$	4''21	GALEX NUV	Marino et al. 2011
2.38×10^{14}	$(2.6 \pm 0.3) \times 10^{-2}$	2''	InfraRed Telescope Facility (IRTF), <i>J</i> band	Becklin et al. 1982
1.87×10^{14}	$(3.5 \pm 0.3) \times 10^{-2}$	2''	IRTF, <i>H</i> band	Becklin et al. 1982
1.35×10^{14}	$(3.2 \pm 0.3) \times 10^{-2}$	2''	IRTF, <i>K</i> band	Becklin et al. 1982
8.47×10^{13}	$(2.8 \pm 0.3) \times 10^{-2}$	2''	IRTF, <i>L</i> band	Becklin et al. 1982
8.3333×10^{13}	4.0×10^{-2}	2''4	<i>Spitzer</i> 3.6 μm	This Work
6.6667×10^{13}	3.7×10^{-2}	2''4	<i>Spitzer</i> 4.5 μm	This Work
6.25×10^{13}	$(3.0 \pm 0.4) \times 10^{-2}$	4''	IRTF, <i>M</i> band	Becklin et al. 1982
5.1724×10^{13}	4.7×10^{-2}	2''4	<i>Spitzer</i> 5.8 μm	This Work
3.75×10^{13}	6.9×10^{-2}	2''4	<i>Spitzer</i> 8.0 μm	This Work
3.3333×10^{13}	$(15 \pm 3) \times 10^{-2}$	$\sim 5''5$	<i>Akari</i> /IRC 9 μm , Point Source Catalogue	NASA/IPAC Infrared Science Archive
2.83×10^{13}	$(11.1 \pm 1.6) \times 10^{-2}$	4''	IRTF, <i>N</i> band	Becklin et al. 1982
2.595×10^{13}	$(15.7 \pm 0.2) \times 10^{-2}$	7''4	<i>WISE</i> W3, AllWISE Source Catalog	NASA/IPAC Infrared Science Archive
2.5×10^{13}	$(13.8 \pm 0.2) \times 10^{-2}$	$\sim 30''$	<i>IRAS</i> 12 μm , IRS enhanced products	NASA/IPAC Infrared Science Archive
1.6667×10^{13}	$(38 \pm 0.02) \times 10^{-2}$	$\sim 5''7$	<i>Akari</i> /IRC 18 μm , Point Source Catalogue	NASA/IPAC Infrared Science Archive
1.47×10^{13}	$(46 \pm 7) \times 10^{-2}$	4''	IRTF, <i>Q</i> band	Becklin et al. 1982
1.3582×10^{13}	$(44.3 \pm 0.9) \times 10^{-2}$	$\sim 12''$	<i>WISE</i> W4, AllWISE Source Catalog	NASA/IPAC Infrared Science Archive
1.27×10^{13}	$(41.4 \pm 0.8) \times 10^{-2}$		<i>Spitzer</i> /MIPS 24 μm , IRS enhanced products	NASA/IPAC Infrared Science Archive
1.2×10^{13}	$(42.2 \pm 0.7) \times 10^{-2}$	$\sim 30''$	<i>IRAS</i> 25 μm , IRS enhanced products	NASA/IPAC Infrared Science Archive
5×10^{12}	0.94	$\sim 60''$	<i>IRAS</i> 60 μm , Point Source Catalog v2.1	NASA/IPAC Infrared Science Archive
4.6154×10^{12}	0.84	$\sim 50''$	<i>Akari</i> /FIS 65 μm , Bright Source Catalogue	NASA/IPAC Infrared Science Archive
4.2827×10^{12}	$(73.7 \pm 1.5) \times 10^{-2}$	6''25 \times 5''35	<i>Herschel</i> /PACS 70 μm , Point Source Catalog	NASA/IPAC Infrared Science Archive
3.3333×10^{12}	$(79 \pm 4) \times 10^{-2}$	$\sim 50''$	<i>Akari</i> /FIS 90 μm , Bright Source Catalogue	NASA/IPAC Infrared Science Archive
3×10^{12}	1.22	$\sim 2''$	<i>IRAS</i> 100 μm , Point Source Catalog v2.1	NASA/IPAC Infrared Science Archive
2.1429×10^{12}	1.3 ± 0.4	$\sim 90''$	<i>Akari</i> /FIS 140 μm , Bright Source Catalogue	NASA/IPAC Infrared Science Archive
1.875×10^{12}	0.9	$\sim 90''$	<i>Akari</i> /FIS 160 μm , Bright Source Catalogue	NASA/IPAC Infrared Science Archive
1.8737×10^{12}	0.65 ± 0.18	17''88 \times 11''52	<i>Herschel</i> /PACS 160 μm , Point Source Catalog	NASA/IPAC Infrared Science Archive
6.667×10^{11}	0.941 ± 0.785	15''	JCMT 0.45 mm	Knapp & Patten 1991
3.75×10^{11}	0.412 ± 0.039	17''	JCMT 0.8 mm	Knapp & Patten 1991
2.7273×10^{11}	0.511 ± 0.019	18''5	JCMT 1.1 mm	Knapp & Patten 1991
2.3077×10^{11}	0.563 ± 0.028	19''5	JCMT 1.3 mm	Knapp & Patten 1991
1.5×10^{11}	1.036 ± 0.083	27''5	JCMT 2.0 mm	Knapp & Patten 1991
8.96×10^{10}	2.0 ± 0.5	$\sim 60''$	NRAO 11 m telescope 89.6 GHz, event A 05/1973	Heeschen & Puschell 1983
8.96×10^{10}	1.2 ± 0.5	$\sim 60''$	NRAO 11 m telescope 89.6 GHz, event B 02/1980	Heeschen & Puschell 1983
8.57×10^{10}	0.91 ± 0.24	$\sim 65''$	NRAO 11 m telescope 3.5 mm, average 1968-1973	Heeschen & Conklin 1975
8.57×10^{10}	2.21 ± 0.52	$\sim 65''$	NRAO 11 m telescope 3.5 mm, 07/1973	Heeschen & Conklin 1975
3.16×10^{10}	1.52 ± 0.24	$\sim 3'$	NRAO 11 m telescope 9.5 mm, average 1968-1973	Heeschen & Conklin 1975
3.16×10^{10}	2.86 ± 0.24	$\sim 3'$	NRAO 11 m telescope 9.5 mm, 07/1973	Heeschen & Conklin 1975
3.14×10^{10}	2.9 ± 0.2	$\sim 3'$	NRAO 11 m telescope 31.4 GHz, event A 05/1973	Heeschen & Puschell 1983
3.14×10^{10}	1.7 ± 0.2	$\sim 3'$	NRAO 11 m telescope 31.4 GHz, event B 02/1980	Heeschen & Puschell 1983
2.2×10^{10}	1.62 ± 0.162	7''	ATCA 22 GHz	Ricci et al. 2006
1.55×10^{10}	2.0 ± 0.1	$\sim 6'$	NRAO 11 m telescope 15.5 GHz, event A 05/1973	Heeschen & Puschell 1983
1.55×10^{10}	1.8 ± 0.1	$\sim 6'$	NRAO 11 m telescope 15.5 GHz, event B 02/1980	Heeschen & Puschell 1983
8.6×10^9	2.63	1''	ATCA 8.6 GHz	Tingay et al. 2003
4.8×10^9	2.47	2''	ATCA 4.8 GHz	Tingay et al. 2003
2.5×10^9	1.46	4''5	ATCA 2.5 GHz	Tingay et al. 2003
1.6649×10^9	$(83.1 \pm 1.7) \times 10^{-2}$	1''	VLA 1.66 GHz	Wrobel 1984
1.3851×10^9	$(73.5 \pm 1.5) \times 10^{-2}$	1''	VLA 1.39 GHz	Wrobel 1984
4.08×10^8	0.84 ± 0.04		Molonglo Radio Telescope 408 MHz	Large et al. 1981
3.65×10^8	0.64		Texas Interferometer 365 MHz	Douglas et al. 1996
7.38×10^7	0.85 ± 0.13	$\sim 80''$	VLA 74 MHz	Cohen et al. 2007

APPENDIX B: OBSERVATION LOG

Table B1. Log of the VLTI/MIDI campaign for NGC 1052. The columns in the table correspond to: the time at which the science target fringes were scanned, the total number of frames within the scan (NDIT), the projected baseline length (BL), the baseline position angle (PA), the quality of the interferometric measurement (good: 1, bad: 0), the number of good frames in the scan (NGOOD), the time of the calibrator fringe scan (Caltime), and the difference in airmass between the science target and the calibrator (Δ am).

Time	Fringe track		PA	FT QC		Calibration	
	NDIT	BL [m]		Q	NGOOD	Caltime	Δ am
2014-08-06: U1U2							
08:08:11	8000	51	10°	0	303	07:49:36	-0.1
08:15:59	8000	51	11°	0	1231	07:49:36	-0.2
08:20:52	16000	51	12°	0	941	07:49:36	-0.2
08:36:02	12000	51	14°	0	2374	08:56:10	0.0
08:42:13	12000	51	15°	1	775	08:56:10	0.0
09:26:18	8000	53	21°	1	2846	09:53:16	0.0
09:31:06	12000	53	21°	1	8475	09:53:16	0.0
09:36:22	12000	53	22°	0	7209	09:53:16	0.0
09:42:24	12000	53	23°	1	3970	09:53:16	0.0
10:14:01	8000	54	26°	0	2685	10:31:19	0.0
10:17:48	8000	54	26°	0	5003	10:31:19	0.0
10:21:51	12000	54	27°	1	8051	10:31:19	0.0
2014-08-07: U1U4							
09:31:24	8000	124	58°	0	1632	09:20:26	-0.0
09:35:29	12000	124	58°	1	3490	09:20:26	-0.0
09:41:18	12000	125	59°	1	4750	09:20:26	-0.0
10:15:08	8000	128	61°	0	1938	10:03:49	-0.0
10:19:44	12000	129	61°	0	230	10:03:49	-0.0
10:28:15	8000	129	62°	0	345	10:03:49	-0.0
2014-11-02: U1U4							
02:56:27	8000	114	53°	0	622	02:37:43	-0.1
03:00:52	8000	115	54°	0	557	02:37:43	-0.1
03:05:35	8000	116	54°	0	931	02:37:43	-0.1
03:37:51	8000	122	57°	0	1323	03:54:07	0.0
03:42:02	8000	123	58°	0	1218	03:54:07	0.0
03:45:51	8000	123	58°	0	1062	03:54:07	-0.0
04:08:09	8000	126	59°	0	361	03:54:07	-0.0
04:11:58	8000	127	60°	0	325	03:54:07	-0.0
04:16:05	8000	127	60°	0	1007	03:54:07	-0.0
04:19:54	8000	127	60°	0	196	03:54:07	-0.0
04:23:51	8000	128	60°	0	624	03:54:07	-0.0
2014-11-03: U2U3							
03:05:30	8000	42	32°	0	796	02:22:14	-0.1
2014-11-03: U3U4							
05:12:34	8000	60	112°	0	1146	05:21:24	0.0
05:36:56	8000	58	114°	0	411	05:21:24	0.0
05:40:53	8000	57	114°	0	457	05:21:24	0.0
2014-11-04: U3U4							
07:30:09	8000	43	128°	0	4053	07:12:53	0.2
07:33:38	8000	42	129°	1	4736	07:12:53	0.2
07:37:12	8000	42	130°	1	5039	07:12:53	0.2
07:58:36	8000	38	135°	0	193	08:14:20	0.0
08:02:25	8000	38	136°	1	3981	08:14:20	0.0
08:06:11	8000	37	137°	1	5169	08:14:20	0.1
08:24:55	8000	35	142°	0	253	08:14:20	0.3
08:28:23	8000	34	143°	0	225	08:14:20	0.3
08:32:15	8000	34	145°	0	1677	08:14:20	0.4